APPLIED SCIENCES AND ENGINEERING

Synthetic networks with tunable responsiveness, biodegradation, and molecular recognition for precision medicine applications

John R. Clegg[1], Afshan S. Irani[1], Eric W. Ander[2], Catherine M. Ludolph[2], Abhijeet K. Venkataraman[1], Justin X. Zhong[2], Nicholas A. Peppas[1,2,3,4,5]*

Formulations and devices for precision medicine applications must be tunable and multiresponsive to treat heterogeneous patient populations in a calibrated and individual manner. We engineered modular poly(acrylamide-co-methacrylic acid) copolymers, cross-linked into multiresponsive nanogels with either a nondegradable or degradable disulfide cross-linker, that were customized via orthogonal chemistries to target biomarkers of an individual patient's disease or deliver multiple therapeutic modalities. Upon modification with functional small molecules, peptides, or proteins, these nanomaterials delivered methylene blue with environmental responsiveness, transduced visible light for photothermal therapy, acted as a functional enzyme, or promoted uptake by cells. In addition to quantifying the nanogels' composition, physicochemical characteristics, and cytotoxicity, we used a QCM-D method for characterizing nanomaterial degradation and a high-throughput assay for cellular uptake. In conclusion, we generated a tunable nanogel composition for precision medicine applications and new quantitative protocols for assessing the bioactivity of similar platforms.

INTRODUCTION

In 2015, the Obama administration launched the precision medicine initiative (*1*). An emerging engineering challenge within precision medicine is the need for versatile platform technologies that can be tailored to individual patients or pathologies (*1*, *2*). A common approach within the fields of biomaterials and nanotechnology has been to design highly tailored formulations that target specific cell and tissue characteristics of a single pathology. These formulations, which can be fabricated in a variety of supramolecular structures [i.e., linear polymer conjugates (*3*), gels (*4*, *5*), and self-assembled materials (*6*, *7*)], recognize hallmark overexpressed cellular markers for the purpose of disease targeting. Nanoparticle carriers for precision medicine applications are typically dynamic in nature, swelling and/or degrading in intracellular environments to deliver therapeutic payloads to the cytosol of target cells (*8*).

In cancer treatment, there is precedence that multiple therapeutics can act synergistically to target and kill tumors. Chemotherapeutic agents act through a variety of mechanisms, including, but not limited to, DNA intercalation, enzyme inhibition, and cell cycle arrest (*9*, *10*). Targeted agents, such as monoclonal antibodies, alter cell signaling pathways and engage the immune system. Photothermal therapy leads to tumor reduction by increasing membrane fluidity (~43°C) or ablating the cells (~50°C) (*11*). All of these therapeutic modalities benefit from targeting strategies, which concentrate the therapeutic agent within the tumor.

Each therapeutic option has distinct potential to aid in an individual patient's treatment regimen. But, there is also marked variability between patients, necessitating precise and tailored treatments specific for the genetic and biophysical properties of the individual pathology. Advancements in genomic and proteomic technologies have made the collection of these relevant individual data a reality. The major hurdles left to overcome include, first, establishing predictive models of patients' response to treatment and, second, engineering highly tunable platform technologies that deliver multiple therapeutic modalities in a patient-specific manner. Our modular strategy addresses the latter challenge and could serve as a useful tool in future studies on the former.

Previous studies on nanoparticle development for cancer precision medicine have focused on highly specified platforms that efficiently target and kill a single tumor population. For example, Conde *et al.* (*12*) recently designed a composite platform composed of gold nanorods, gold nanoparticles, therapeutic antibodies, and small interfering RNA encapsulated within an adhesive hydrogel patch. This system targeted and killed colorectal cancer cells through multiple modalities (i.e., photothermal therapy, RNA interference, and targeted chemotherapy), increasing treatment efficacy in vitro and in vivo.

In another illustrative example, Liu *et al.* (*13*) constructed a hierarchical nanomaterial assembly that delivered a cytotoxic protein (ribonuclease A) and antibiotic (doxycycline). This platform targeted cancer stem cells within heterogeneous cancer populations. The targeted, dual therapy led to a significant reduction in tumor volume relative to both the controls and individually administered therapeutics. These are only two examples, out of many promising studies on cancer nanomedicines that have used multiple therapeutic modalities (*12*–*15*). There is a need, therefore, for a readily modifiable platform that facilitates the rapid customization of cancer nanomedicines to individual patients' pathologies.

We previously demonstrated the ability to tune the hydrodynamic diameter and magnitude of pH response of poly(acrylamide-co-methacrylic acid) [P(AAm-co-MAA)] nanogels by modulating the monomer feed, polymerization parameters, or purification strategy (*16*). In the present work, our "base" platform is this random P(AAm-co-MAA) copolymer cross-linked into a nanogel with either a nondegradable or a redox-labile cross-linker. We present a new, modular sequence of nanogel modifications with small molecules, peptides, or proteins; these nanogels are multifunctional and multiresponsive, exhibiting dynamic loading and release of therapeutic payloads, engaging

[1]Department of Biomedical Engineering, The University of Texas at Austin, Austin, TX, USA. [2]McKetta Department of Chemical Engineering, The University of Texas at Austin, Austin, TX, USA. [3]Institute for Biomaterials, Drug Delivery, and Regenerative Medicine, The University of Texas at Austin, Austin, TX, USA. [4]Division of Molecular Pharmaceutics and Drug Delivery, College of Pharmacy, The University of Texas at Austin, Austin, TX, USA. [5]Department of Surgery and Perioperative Care, and Department of Pediatrics, Dell Medical School, The University of Texas at Austin, Austin, TX, USA.
*Corresponding author. Email: peppas@che.utexas.edu

in a bioactive manner with biological substrates, transducing external signals into therapeutic heating, and promoting cellular internalization.

To achieve modular functionalization while retaining the bioactivity of conjugated molecules, we rely on facile and biocompatible conjugation schemes. While there are numerous bioconjugation strategies documented in the literature (*17*–*19*), we use carbodiimide-mediated coupling to attach diverse ligands to pendant carboxylic acid groups via a stable amide bond. In this coupling scheme, carboxylic acid groups are activated with a catalyst to form a reactive ester intermediate, which is highly reactive with primary amines in slightly acidic aqueous solutions. We can, therefore, couple any water-soluble, amine-terminated molecule—including, but not limited to, proteins, peptides, and small molecules—directly to our polymer backbone. The diversity of bifunctional linker molecules that are available commercially, such as poly(ethylene glycol) derivatives (*20*, *21*), further diversifies the ligands that our platform can accommodate, including those with amine, carboxylic acid, hydroxyl, or sulfhydryl groups.

We hypothesized that a single platform, when modified in a modular manner with bioactive components, could respond dynamically to tumor physiological environments, partition and elute therapeutic agents in a controlled manner, transduce external signals for therapeutic heating, and target tumor populations. We believe that this platform—which can be modified to achieve environmental responsiveness, therapeutic delivery, and molecular recognition—is an enabling technology for delivering personalized and calibrated combination therapies. A summary schematic for our platform, along with the reagents, chemical modifications, and therapeutic modalities explored, is given in Fig. 1. In this proof-of-concept study, we demonstrate how a single, biocompatible platform can be quickly and precisely modified for personalized and precision medicine applications. Furthermore, in addition to standard characterization techniques, we developed and applied two new experimental methods: a quartz crystal microbalance with dissipation (QCM-D) assay for nanogel degradation and a high-throughput cell imaging assay for determining the kinetics of nanogel uptake. These new techniques expand upon the field's repertoire of experimental methods for evaluating and comparing new nanoparticle systems for precision medicine.

RESULTS

P(AAm-co-MAA) nanogel platform

Our base platform for small molecule–modified nanogels was an ionomer collapse–purified P(AAm-co-MAA) nanogel, synthesized as described by Zhong *et al.* (*16*). These nanogels had a swollen hydrodynamic diameter of 76 ± 8 nm, were 63% acidic copolymer by mass, and exhibited pH-responsive expansion/syneresis behavior with a critical pH transition point of 4.8. Ionomer collapse–purified nanogels, as opposed to those purified by dialysis alone, were selected because the basic conditions (0.5 N sodium hydroxide) are known to induce hydrolysis of some of the nanogel acrylamide content to acrylic acid, providing additional acid groups for bioconjugation. The

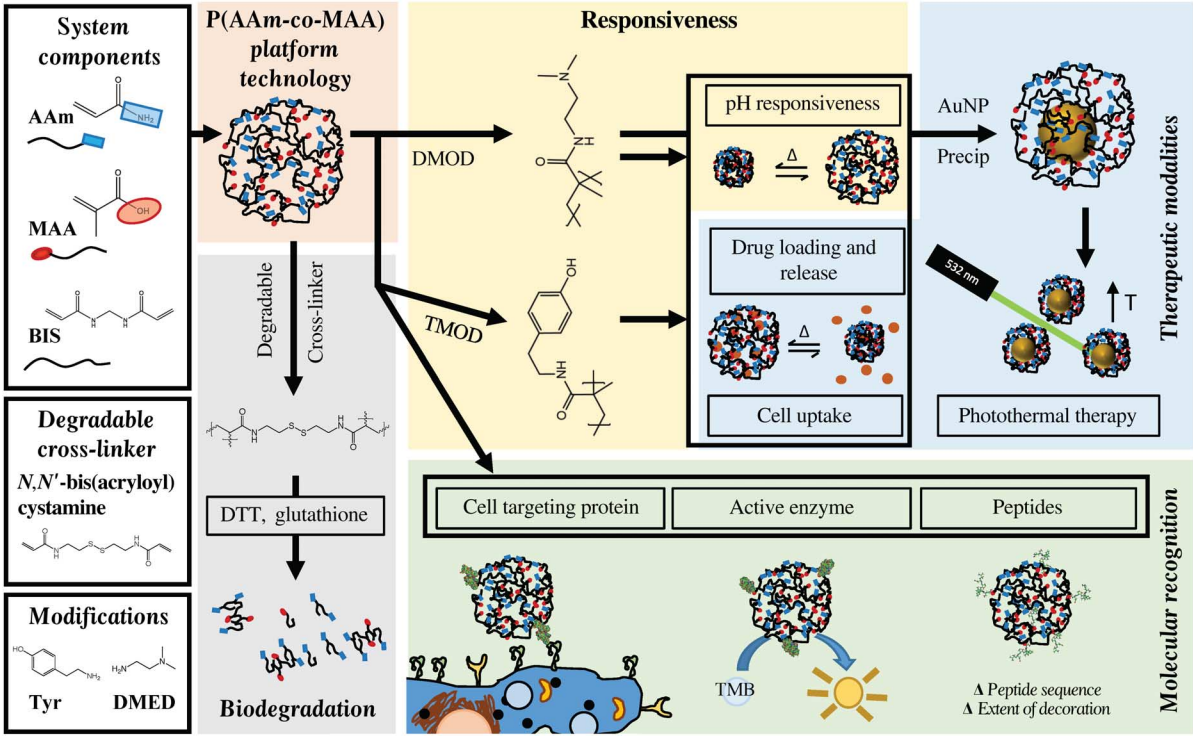

Fig. 1. Overview of the P(AAm-co-MAA) nanogel platform and the use of its derivatives for precision medicine applications. Nanoscale networks of acrylamide (AAm) and methacrylic acid (MAA), cross-linked with methylenebisacrylamide (BIS) or its degradable disulfide analog [*N*,*N*′-bis(acryloyl)cystamine], were synthesized by inverse emulsion polymerization and modified via carbodiimide chemistry with tyramine (Tyr), *N*,*N*-dimethylethylenediamine (DMED), proteins, or peptides. In an additional post-synthesis step, gold nanoparticles (AuNP) were precipitated within DMED-modified (DMOD) nanogels. Here, we document the synthesis and modification of this nanogel platform and demonstrate the impact of nanogels' modification on their ability to respond to the pH environment, load and release a model cationic drug, target cells, act as a functional enzyme, and transduce green light for photothermal therapy. Because of its tunability and the variety of therapeutic modalities enabled, we believe that this platform is suitable for precision medicine applications. DTT, dithiothreitol; TMB, 3,3′,5,5′-tetramethylbenzidine.

increased presence of carboxylic acids allowed us to couple a greater quantity of functional small molecules to each nanogel.

Biodegradation

An additional degree of tunability was introduced to the P(AAm-co-MAA) nanogels by introducing a biodegradable cross-linker. *N*,*N*′-bis(acryloyl)cystamine is a bisacrylamide analog that contains a labile disulfide linkage. It has been used previously as a component of digestible gels for drug and gene delivery applications (*22*–*24*). We successfully cross-linked P(AAm-co-MAA) nanogels with *N*,*N*′-bis(acryloyl)cystamine. These biodegradable nanogels were similar in hydrodynamic diameter, zeta potential, and pH-responsiveness to their nondegradable analogs (fig. S1).

The kinetics and mechanisms of biodegradation for these nanogels were quantified by optical and gravimetric analyses. Optical analysis was conducted via dynamic light scattering (DLS) with a fixed detector position and signal attenuation. Under these measurement conditions, the count rate is related to the decrease in the number of suspended nanoparticles (*25*). Simultaneously, the hydrodynamic diameter measurements collected provide inference to the mechanism of biodegradation (i.e., surface erosion and bulk degradation). We assessed biodegradation by DLS for degradable nanogels in the presence of 10 mM dithiothreitol (DTT) or glutathione in 1× phosphate-buffered saline (PBS) at pH 7.4. DTT is a common reducing agent used for biological applications. It has been used previously to degrade systems cross-linked with *N*,*N*′-bis(acryloyl)cystamine and was selected to ensure that the nanogels degrade completely. Glutathione (10 mM) in 1× PBS was selected as a biologically relevant reducing condition, as it mimics the intracellular environment (*26*).

The chemical mechanism of nanogel degradation by each reducing agent, as well as a pictorial depiction of the biodegradation process, is given in Fig. 2A. DLS analysis confirmed that both DTT and glutathione were able to reduce the disulfide cross-linker and consequently degrade the nanogel network (Fig. 2B). In the presence of DTT, the nanogels degraded rapidly and were indistinguishable from a linear polymer solution of the same concentration (i.e., completely degraded) after 40 min. Nanogels degraded with reduced kinetics in a 10 mM glutathione solution. The normalized count rate declined by 72.0 ± 5.8% after 50 min in glutathione solution, and the nanogels were indistinguishable (by DLS count rate) from linear polymer after 48 hours.

In QCM-D experiments, the nanogels were covalently conjugated to a gold-coated quartz sensor, and the mass loss, under reducing

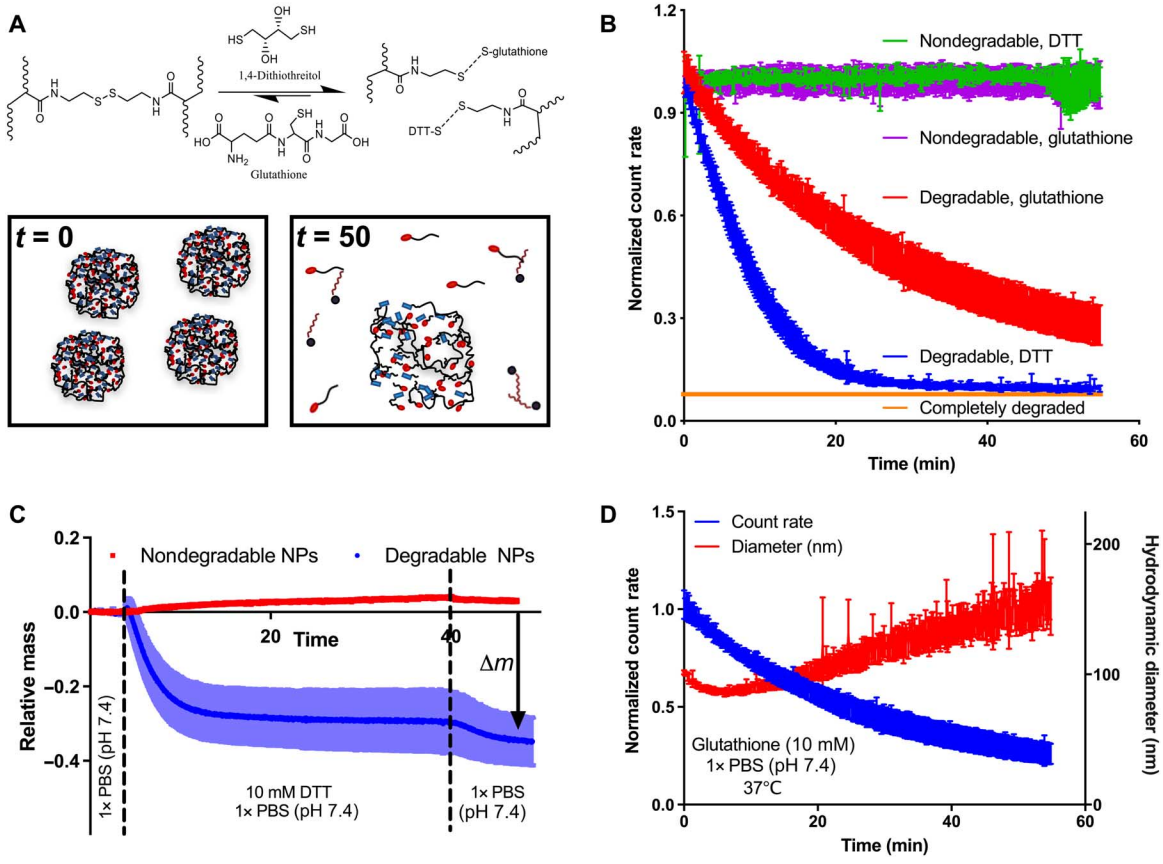

Fig. 2. Nanogel biodegradation analysis by DLS and QCM. (**A**) *N*,*N*′-bis(acryloyl)cystamine cross-linked nanogels degrade via reduction of the disulfide. The diagram demonstrates how, after an initial period of surface erosion, the nanogels experience bulk degradation, leading to simultaneous network swelling. (**B**) DLS analysis of nanogel degradation. While bisacrylamide cross-linked nanogels did not degrade under reducing conditions, those cross-linked with a disulfide cross-linker were digested by both reducing agents (n = 4, mean ± SD). (**C**) QCM analysis demonstrated the kinetic decomposition of nanogels under reducing conditions and flow. While the mass of nondegradable nanogels was relatively unaffected by reducing conditions, the mass of degradable gels declined rapidly (n = 3, mean ± SD). (**D**) Hydrodynamic diameter analysis by DLS supported the degradation mechanism of initial surface erosion followed by bulk degradation. While the normalized count rate declined steadily throughout the extended measurement, the hydrodynamic diameter decreased initially (surface erosion) and then increased for the remainder of the experiment (i.e., decrease in cross-links led to a reduction in the total number of nanoparticles but swelling of the remaining intact nanogels) (n = 3, mean ± SD).

conditions, was monitored by measuring the change in the quartz sensor's fifth harmonic resonance frequency (*27*). Mass loss was normalized to the initial mass of coupled nanogels to determine a relative measure. It is noteworthy that because the nanogels are covalently conjugated to the quartz sensor, the mass loss will never reach 100%. Some linear polymer strands will remain immobilized on the sensor following complete degradation of the cross-links.

Under a steady flow of fresh 10 mM DTT (1× PBS, pH 7.4), the mass of nondegradable nanogels increased slightly. This increase was likely due to adsorption of DTT molecules. On the other hand, the relative mass of degradable nanogels decreased rapidly, reaching a degraded state in 15 min (Fig. 2C). As shown in fig. S2, in parallel with an increasing resonance frequency, the dissipation of sensors coated with degrading increased. This indicated that as the nanogels were degrading, they were simultaneously losing mass and imbibing water. This observation was consistent with our DLS measurements, which showed that the nanogels simultaneously degraded and swelled under reducing conditions (Fig. 2D).

Physicochemical properties of modular nanoscale hydrogels

Next, we explored the ability to modify the pendant acid groups on P(AAm-co-MAA) with amine-terminated small molecules (tyramine and *N*,*N*-dimethylethylenediamine) to add phenol or tertiary amine groups to the polymer backbone, respectively. Nanogels modified to different extents with tyramine (TMOD) or *N*,*N*-dimethylethylenediamine (DMOD) were characterized by Fourier transform infrared (FTIR spectroscopy), potentiometric titration, DLS, and zeta potential measurement (Fig. 3).

FTIR analysis showed that the small molecules were covalently bound to the nanogel network, as evidenced by the reduction in peaks corresponding with the carboxyl carbonyl (1700 cm^{-1}) and carbon-oxygen single bond (1200 cm^{-1}). A graphical depiction of select formulations is given in Fig. 3A, with the full analysis of all formulations given in fig. S3. From the FTIR analysis, it initially appeared that the DMOD reaction proceeded with greater efficiency, as the disappearance of carboxylic acid peaks was more pronounced. However, potentiometric titration revealed that the percent of modified methacrylic acid moieties trended with the stoichiometric ratio of ligand to carboxylic acid similarly for both ligands (Fig. 3, B and C). Therefore, the trends observed in the FTIR spectra are likely reflective of the location of nanogel modification (surface for DMOD and bulk for TMOD) rather than the efficiency of the reaction. The circled formulations (0.5 TMOD and 0.78 DMOD) in Fig. 3B, which achieved a high degree of efficient molecular coupling, were used in each of the following experiments.

Potentiometric titration, pH-responsive zeta potential, and size measurements for TMOD, DMOD, and unmodified nanogels are also presented in Fig. 3 (C to E). As shown in the potentiometric titration analysis, unmodified nanogels were 63% polyacid [i.e., poly(acrylic acid) and poly(methacrylic acid)] by mass, as compared with 22 and 25% for the TMOD and DMOD nanogels, respectively. The reduction in acid content, because of modification, trended linearly with ligand concentration in the modification reaction at low extents of modification and plateaued at 69.8 ± 3.7% modification. Full potentiometric titration analysis of all TMOD and DMOD formulations is presented in fig. S4.

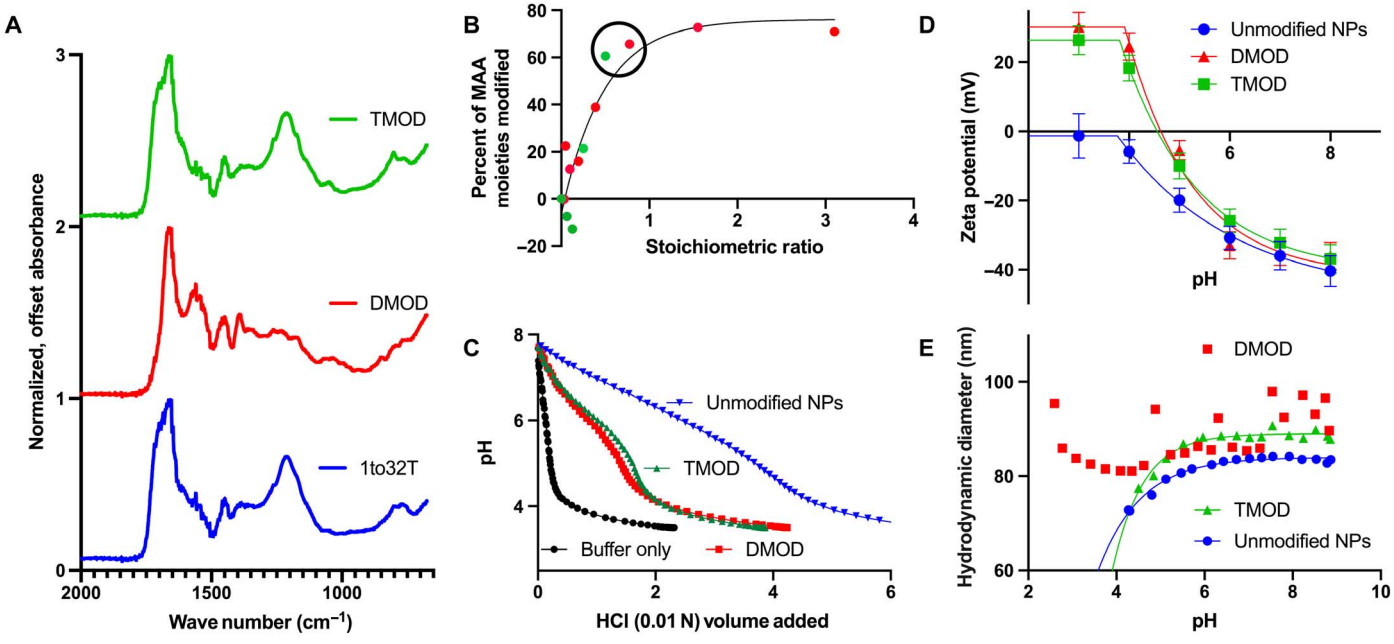

Fig. 3. Characterization of small molecule–modified nanogels. (**A**) FTIR spectra of TMOD and DMOD nanogels, as compared with the unmodified formulation. The peaks at 1700 and 1200 cm^{-1} correspond to the carboxylic acid, at 1660 and 1590 cm^{-1} correspond to the amide, and at 800 cm^{-1} correspond to the aromatic groups, confirming the incorporation of each small-molecule ligand through covalent coupling. FTIR analysis of all formulations is presented in fig. S1. (**B**) Nanogel modification proceeded with approximately 60% efficiency when the ligand concentration did not exceed the carboxylic acid concentration (stoichiometric ratios less than 1). (**C**) Potentiometric titrations were used to quantify the carboxylic acid content of all formulations, elucidating the extent of small-molecule coupling. (**D**) Modified nanogels exhibited a pH-responsive zeta potential transition (anionic to cationic), whereas unmodified nanogels were anionic across all pH values tested ($n = 3$, mean ± SD). (**E**) Unmodified and TMOD nanogels exhibited a pH-responsive collapse with a critical transition point at pH ~ 4.8. DMOD nanogels did not undergo substantial pH-responsive swelling.

All three formulations were anionic at pH values greater than five, as the carboxylic acid groups were predominantly deprotonated [pK_a (where K_a is the acid dissociation constant), ~4.8] and held a negative charge. As the pH was reduced from 8 to 3, the TMOD and DMOD nanogels' zeta potential was less negative than that of unmodified nanogels and became positive at pH 4.7. In this pH environment, as well as those more acidic, the carboxylic acid groups are protonated and therefore uncharged, whereas the tertiary amines contributed by *N*,*N*-dimethylethylenediamine and adsorbed sodium ions from the solution (5 mM sodium phosphate buffer) are positively charged. This pH-responsive ionization change for the modified nanogels is especially critical for environmentally responsive drug delivery, as will be shown in a later section.

The modified and unmodified nanogels' hydrodynamic diameters, as measured by DLS, also changed in response to the pH environment. TMOD and unmodified nanogels exhibited similar pH-responsive collapses, with a critical pH transition of approximately 4.8. As the pH of the solution was dropped below 4, both the TMOD and DMOD nanogels aggregated. For the purpose of visualization, hydrodynamic diameter measurements from aggregated states were omitted from Fig. 3E. The full data are presented in fig. S5.

It is noteworthy that DMOD nanogels exhibited a nearly complete loss of pH-responsive swelling. This can be attributed to the fact that because of the modified network's amphoteric nature, it bears charge across all pH values. Its state of electrical neutrality at pH 4.7 is a result of balanced negatively and positively charged species, rather than a loss of ionization. On the contrary, the pH-responsive behavior of both the unmodified and TMOD nanogels suggests aggregation caused by a hydrophobic transition and loss of ionization. Taken in combination with the observed trends in zeta potential, this suggests that the TMOD nanogels' negative-to-positive charge transition is a result of the association of ionic species, both salts from the buffer and additional tyramine molecules that were neither conjugated nor extracted during purification, rather than the network components themselves bearing a positive charge.

Partitioning and elution of model therapeutics

Suspensions of DMOD, TMOD, and unmodified nanogels were incubated separately with methylene blue in distilled water, and methylene blue loading was achieved through equilibrium partitioning. Methylene blue was selected as a model therapeutic agent because of its cationic nature, use as a photosensitizer, and similarity to the chemotherapeutic 5-fluorouracil. Methylene blue is a hydrophilic compound (log$P$ = −1.1), similar to 5-fluoruracil (log$P$ = −0.89). Methylene blue–loaded nanogels were dialyzed against 1× PBS (of pH 4.5 or 7.4), which was exchanged regularly with fresh buffer to both simulate drug sequestration/metabolism and establish a semi-sink condition. The buffer condition (1× PBS at pH 7.4) was intended to simulate the pH environment in circulation, whereas the pH 4.5 condition was meant to emulate the environment of the late endosome, which nanocarriers will experience during lysosomal trafficking following cellular uptake. It is noteworthy that in the case of cancer drug delivery, the nanocarriers will experience a gradient of pH, decreasing from circulation through the endosomal pathway. The drug release environment was maintained at 37°C, and methylene blue elution was monitored until complete release was achieved (28 hours).

Unmodified nanogels loaded significantly more methylene blue than their TMOD and DMOD derivatives (fig. S6). Prior to modifications, nanogels loaded methylene blue with 99.5 ± 0.3% efficiency (equal mass ratio nanogels: methylene blue in ultrapure water). Increasing nanogel modification with tyramine or *N*,*N*-dimethylethylenediamine decreased the equilibrium partitioning of methylene blue. Specifically, TMOD and DMOD nanogels loaded methylene blue with 59.7 ± 2.1% and 34.9 ± 9.2% efficiency, respectively. This decrease in equilibrium partitioning, relative to unmodified control nanogels, is due to the hydrophobicity or cationic character that the respective ligands contribute. As a cationic and hydrophilic payload, methylene blue enages in complementary electrostatic interactions with deprotonated methacrylic acid groups. Furthermore, as methylene blue partitions preferentially in water over organic phases, we expected loading efficiency to correlate positively with nanogel hydrophilicity. In the preceding section, we showed that the extent of nanogel functionalization correlated with the amount tyramine or *N*,*N*-dimethylethylenediamine in the reaction solution. Furthermore, as each modification reaction depleted a pendant methacrylic acid group, there is a negative relationship between extent of nanogel modification and the available methacrylic acid groups to interact with methylene blue. Following modification with *N*,*N*-dimethylethylenediamine, the amphoteric nanogels lost pH-responsive swelling behavior. Their tertiary amine moieties, which are cationic, exerted a repulsive force on methylene blue. As a result of tyramine modification, the nanogels became more hydrophobic, similarly lowering the networks' ability to partition methylene blue. These physicochemical characteristics of TMOD and DMOD nanogels are useful for responsive release behavior, but as they decrease the nanogel–methylene blue affinity, they decrease methylene blue loading efficiency.

A drug release experiment probed the ability of each modified or unmodified nanogel system to act as an intelligent drug delivery vehicle. In this experiment, nanogels loaded with methylene blue [nanogels (1 mg/ml), with corresponding loading described above] were placed in dialysis tubing [regenerated cellulose, molecular weight cutoff (MWCO), 12,000 to 14,000 kDa] and dialyzed against 1× PBS (pH 4.5 or 7.4). The dialysate was exchanged for fresh buffer every 2 hours to simulate drug metabolism. At each time point, a sample was taken from both within the dialysis tubing and outside it (i.e., the dialysate) to ensure precise measurement of the kinetic methylene blue release.

Unmodified nanogels exhibited sustained-release kinetics without a noticeable burst release or pH-responsiveness. In 2 hours, unmodified nanogels eluted 41.0 ± 15.5% and 46.0 ± 4.0% of their loaded methylene blue at pH 7.4 and 4.5, respectively (Fig. 4A). The unmodified nanogels' consistency, in their rate of methylene blue elution between the two pH environments, is consistent with their continuously anionic zeta potential. While the pH 4.5 environment is below the unmodified nanogels' pK_a, sufficient acid moieties remained deprotonated to engage in electrostatic interactions with methylene blue and promote payload retention in a manner similar to the pH 7.4 condition.

On the other hand, TMOD nanogels exhibited an initial burst release, which varied significantly with the pH environment (78.5 ± 9.6% and 43.7 ± 18.9% of the loaded payload in the first 15 min, at pH 4.5 and 7.4, respectively; $P < 0.05$). After the burst release, TMOD nanogels gradually released methylene blue at pH 7.4 and rapidly released it at pH 4.5 (Fig. 4B). TMOD nanogels bear a cationic zeta potential in acidic buffers and further undergo a hydrophile-to-hydrophobe transition around the critical pH point (pH 4.8). These physical and chemical alterations, which were unique to the TMOD nanogels, explain their significant and unique pH-responsive methylene blue release profile. DMOD nanogels exhibited substantial burst release, followed by rapid methylene blue elution at both pH 4.5 and 7.4 (Fig. 4C). Methylene blue release was more rapid from DMOD nanogels at pH 4.5 than pH 7.4,

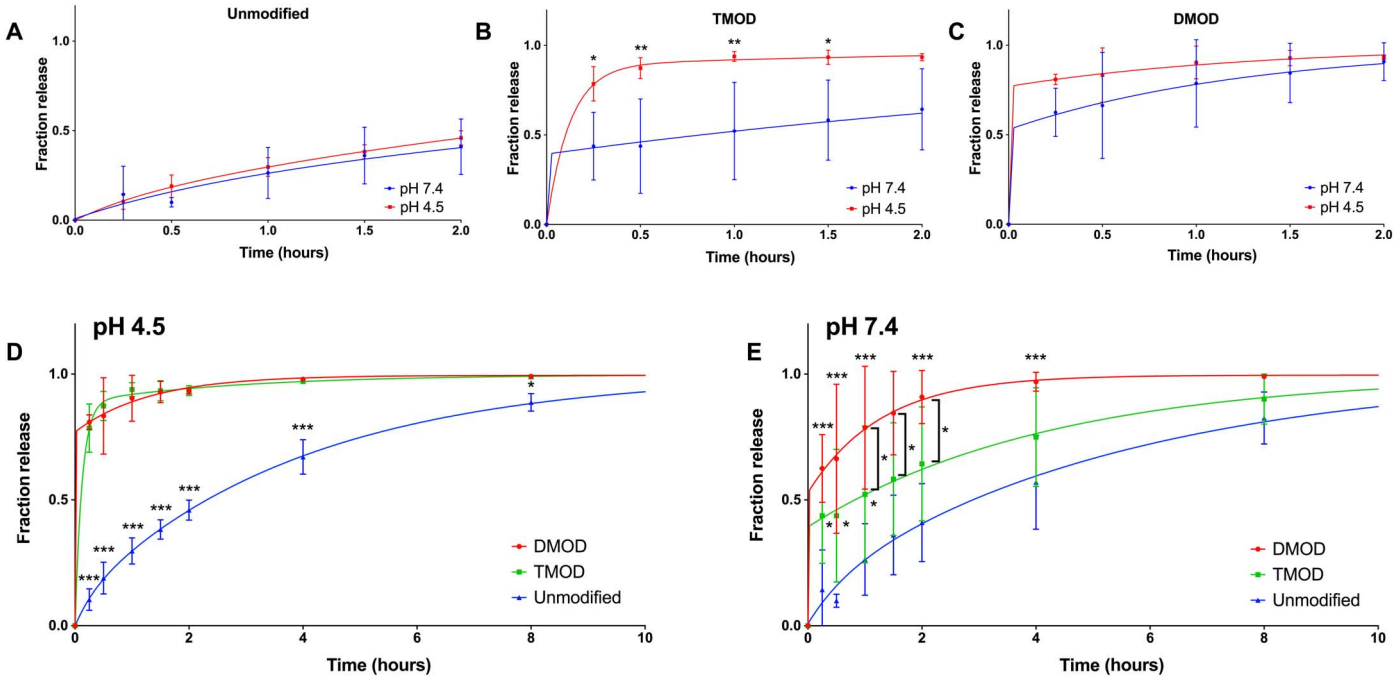

Fig. 4. Model drug (methylene blue) release from modified and unmodified nanogels. (**A**) Methylene blue experienced complementary electrostatic interactions with unmodified nanogels at both pH 4.5 and 7.4, leading to sustained release in both conditions. (**B**) TMOD nanogels exhibited an initial burst release of methylene blue, where the quantity of that release was greater in acidic than neutral conditions. (**C**) DMOD nanogels exhibited a burst release of greater than 50% the loaded payload in each pH condition, with more rapid release in acidic than neutral conditions. (**D**) DMOD and TMOD nanogels exhibited similar methylene blue release behavior in acidic conditions, while unmodified gels exhibited a more sustained-release profile. (**E**) DMOD nanogels released methylene blue rapidly in 1× PBS (pH 7.4), while unmodified nanogels exhibited sustained-release and TMOD gels displayed intermediate behavior. The results in (D) and (E) indicated that the nanogels' zeta potential is largely predictive for their release profile [all panels: $n = 4$, mean ± SD; $^{*}P < 0.05$, $^{**}P < 0.01$, and $^{***}P < 0.001$, two-way analysis of variance (ANOVA) with Tukey posttest].

which can be attributed to the transition from anionic to cationic zeta potential, as was shown previously.

Figure 4 (D and E) highlights the differences in pH-responsive methylene blue elution for the three formulations. All nanogel formulations eluted the entirety of the methylene blue payload within 28 hours. Unmodified nanogels exhibited a sustained-release profile in both pH conditions, demonstrating their use for controlled release but lack of responsive release. DMOD nanogels, conversely, released methylene blue rapidly in both pH environments, acting as neither a sustained-release depot nor a responsive delivery vehicle. TMOD nanogels acted as a pH-responsive delivery vehicle, responding to the acidic environment by rapidly releasing methylene blue. In the pH 4.5 environment, there were significant differences ($P < 0.001$) between the relative elution of methylene blue from modified and unmodified nanogels. However, there were no differences between the methylene blue elution profiles of the DMOD and TMOD nanogels. This indicated that the release profile is driven primarily by the nanogels' cationic zeta potential and not a hydrophile-to-hydrophobe transition (which was unique to TMOD). In the pH 7.4 environment, there were significant differences between the methylene blue elution profile of all three formulations.

These results illustrated how modification of the acid moiety, through changing the nanogels' environmentally responsive swelling and ionization, altered the systems' use as a drug delivery vehicle. While unmodified nanogels were most advantageous for steadily delivering a hydrophilic, cationic payload to the surrounding environment, TMOD nanogels exhibited rapid pH-responsive delivery. This pH responsiveness could lead to triggered release in the acidic tumor or endosome microenvironments. Therefore, the identity and extent of nanogel surface modifications should be carefully tuned to yield combinations of sustained and responsive release for specific drug delivery applications.

Cytotoxicity

Our original design goal was to construct a tunable nanoscale hydrogel platform that was cytocompatible and could be diversified in a modular manner with bioactive moieties. To assess cytotoxicity, we incubated nanogels with murine fibroblasts for 24 hours and measured the impact of nanomaterial exposure on the cells' membrane integrity and metabolic activity.

Intact nanogels (degradable and nondegradable) exhibited limited toxicity to fibroblasts after 24 hours of incubation, while nanogels degraded by 10 mM glutathione in cell culture medium were nontoxic at concentrations up to 2 mg/ml (fig. S7A). Fibroblast membrane integrity was largely unaffected by 24-hour incubation with nondegradable, degradable, or degraded nanoparticles (fig. S7B), indicating that the reduction in metabolic activity observed in fig. S7A was not due to cell lysis. Modification of nanogels with tyramine or *N*,*N*-dimethylethylenediamine did not alter their cytotoxicity (fig. S7C), as measured by cell metabolic activity following 24-hour exposure to a dose of 2 mg/ml. Peptide incorporation (fig. S7D) at approximately 2 weight % (wt %) of the dry nanogel weight did not significantly affect nanogel cytotoxicity (fibroblasts, 24-hour exposure, 2 mg/ml dose), as peptide-modified nanogels did not alter the cells' metabolic activity.

We then monitored the extent to which nanogel toxicity differed across different cell types (fibroblast, macrophage, and colon epithelial).

These were selected as model cell systems for the different cell types that would experience a nanomaterial insult following injection. We recognized that each cell line would interact with the nanogels differently, altering the extent to which the material impairs the cell viability. No significant differences were observed in the cells' viability, as determined by metabolic activity or membrane integrity, for degradable, nondegradable, or degraded nanogels at concentrations up to 2 mg/ml (fig. S8). It is noteworthy that we saw a nonstatistically significant trend in macrophage activity, where metabolic activity increased and membrane integrity decreased at the top concentration (2 mg/ml, 24 hours). This does indicate acute toxicity to macrophages at this dose.

Cell interaction and nanogel uptake

We assessed the impact of the nanogels' chemistry, through surface modification, on their uptake by different model cell lines. We selected fibroblasts, macrophages, and epithelial cells because they model components of the connective tissue, immune system, and tissues/organs, respectively. Furthermore, by selecting colon epithelial carcinoma (SW-48) cells as the epithelial model, we simultaneously probed the impact of surface modification on preferential uptake by human tumor cells.

Modified nanogels for uptake studies were prepared in the same manner as in previous modification efficiency, therapeutic efficacy, and cytotoxicity studies, except for the addition of a carboxylic acid–reactive fluorophore in the modification solution. To make the nanogels fluorescent, we added 5-(aminoacetamido)fluorescein at 0.8 wt % of the dry polymer (for comparison, the tyramine or *N*,*N*-dimethylethylenediamine ligand was added simultaneously at 10 wt %) to the modification solution. This fluorophore was conjugated to all of the nanogel formulations, including the unmodified nanogels.

The fluorophore was successfully conjugated to unmodified, TMOD, and DMOD nanogels, although a decreased fluorophore coupling efficiency was observed for DMOD nanogels. We produced calibration curves for all modified nanogel formulations and normalized our subsequent image analyses to the relative slope for each formulation (correction factors: unmodified, 1.27; TMOD, 1; and DMOD, 5.44). We also validated that fluorophore conjugation did not significantly alter the nanogels' cytotoxicity by conducting MTS [3-(4,5-dimethylthiazol-2-yl)-5-(3-carboxymethoxyphenyl)-2-(4-sulfophenyl)-2H-tetrazolium] and LDH (lactate dehydrogenase) assays for nanogel exposure to each of the three cell lines at concentrations up to 2 mg/ml. No significant cytotoxicity was observed by either measure at concentrations up to 1 mg/ml (24-hour exposure, all three cell lines) (fig. S9). Consequently, the maximum nanoparticle dose for all uptake studies was maintained at 1 mg/ml.

Even at low doses (less than 40 μg/ml, 24-hour exposure), murine macrophages imbibed substantial quantities of all three nanogel formulations (Fig. 5, A to C). On the other hand, fibroblasts exhibited limited uptake of unmodified and TMOD but took up DMOD nanogels. Human colon epithelial cells took up all three formulations, exhibiting no preference for unmodified or TMOD nanogels, but a 13.4-fold increase in uptake when exposed to DMOD nanogels (relative to unmodified nanogels, 250 μg/ml, 24-hour exposure). Representative images, visualizing nanogel uptake by each of the three cell lines, are given in fig. S10.

These dose-response results demonstrated that, while nanogel modification with *N*,*N*-dimethylethylenediamine generally increased uptake, the extent to which uptake was enhanced differed between cell lines. Compared with unmodified nanogels, DMOD nanogels exhibited a 4.5-fold increase in uptake by macrophages, 11.6-fold by fibroblasts,

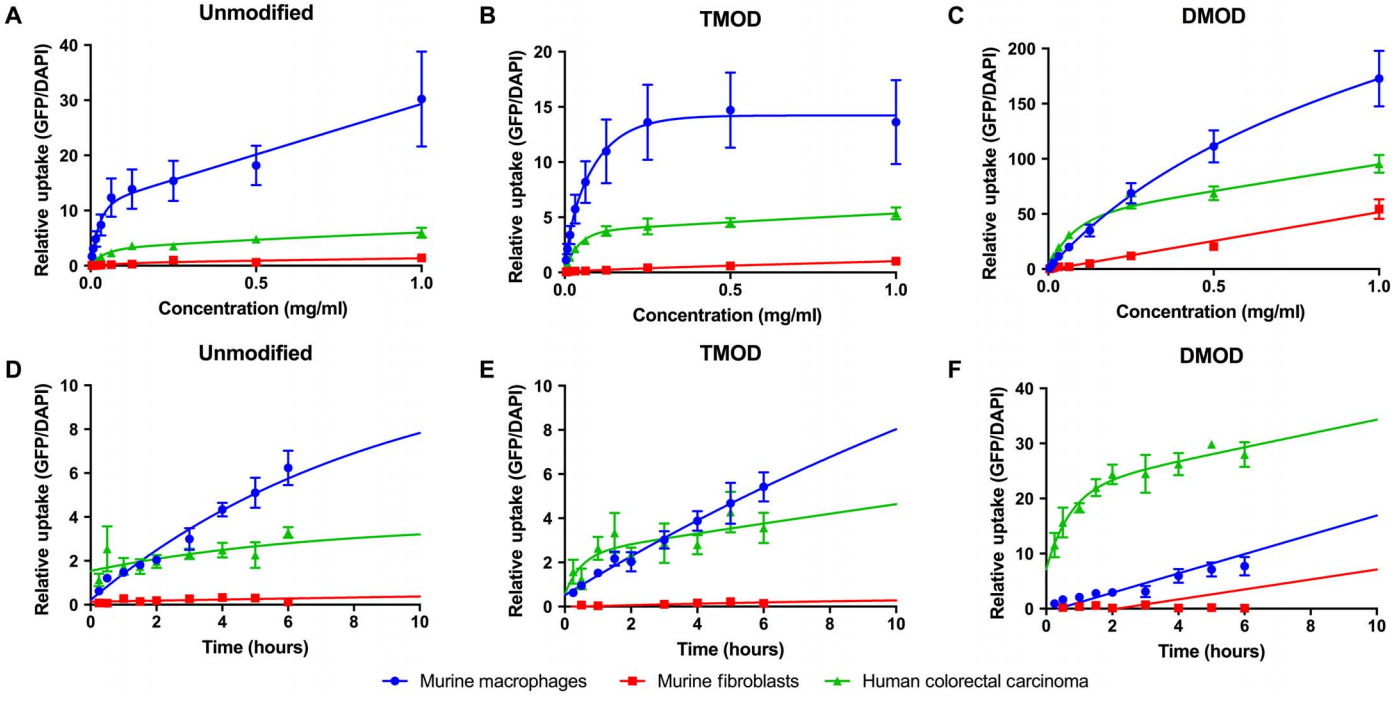

Fig. 5. Relative uptake of unmodified, TMOD, and DMOD nanogels by murine fibroblasts, murine macrophages, and human colon epithelial carcinoma cells. The relative uptake was computed by normalizing the green fluorescent protein (GFP) (nanoparticle) signal to the slope of the calibration curve and then normalizing that value to the 4′,6-diamidino-2-phenylindole (DAPI) (cell nucleus) signal. Note that the *y* axis quantities differ between plots, as the DMOD nanogels were uptaken in significantly greater quantity than TMOD or unmodified nanogels. (**A** to **C**) Relative uptake of unmodified, TMOD, or DMOD fluorescent nanogels by each cell line, as a function of dose (24-hour exposure). (**D** to **F**) Kinetic uptake of unmodified, TMOD, and DMOD nanogels (400 μg/ml dose). Representative images for each plot are given in fig. S10 (all panels, $n = 4$, mean ± SEM).

and 17.0-fold by colon carcinoma cells (250 μg/ml, 24-hour exposure, all differences significant at the $P < 0.05$ level). This result suggests that the cell-nanomaterial interactions, which promoted uptake and were imparted by the *N*,*N*-dimethylethylenediamine moiety, triggered varying degrees of response from different cells. Furthermore, TMOD nanogels were uptaken similarly to unmodified nanogels. Tyramine modification led to a 21% decrease in uptake by macrophages, 31% decrease by fibroblasts, and 3.8% increase by colon carcinoma cells, none of which were statistically significant. This confirmed that a surface modification that imparts environmental responsiveness or alters therapeutic partitioning does not necessarily also enhance cell uptake.

Image analysis revealed that the nanogels interacted with each cell line in a different spatiotemporal manner. Nanogels did not interact substantially with fibroblasts, and when they did, they colocalized primarily with the cell membrane. Macrophages rapidly internalized the nanogels, with images demonstrating cytosolic colocalization in as little as 30 min. In the case of colon epithelial cells, nanogels first associated with the cell membrane, which preceded uptake. DMOD nanogels associated with the colon epithelial cells' membranes and were internalized more rapidly than unmodified and TMOD nanogels (fig. S10).

Kinetic analyses of nanogel uptake further clarified the differences in nanogel uptake within cell lines and between formulations (Fig. 5, D to F). For precision medicine applications, we want to ensure that target cells (i.e., colon cancer cells) internalize the nanomaterial prior to complete therapeutic elution or clearance by off-target cells (i.e., fibroblasts or macrophages). It is relevant to recall that, depending on the particular surface modification and pH environment, the majority of the loaded methylene blue was eluted in less than 4 hours. Therefore, a formulation that rapidly associates with, and facilitates uptake by, target cells will enhance cytosolic delivery of the payload.

Murine macrophages took up all three nanogel formulations with near zero-order kinetics for the first 6 hours. On the other hand, colon carcinoma cells exhibited a rapid cell-nanoparticle association [i.e., a spike in the green fluorescent protein (GFP)/4′,6-diamidino-2-phenylindole (DAPI) signal in the first 15 min to 2 hours], followed by a plateau in the signal intensity. Nanogels did not associate with the membrane or cytosol of murine fibroblasts until 24 hours of exposure. We looked specifically at nanogel uptake within the first 2 hours of dosing, as this is when majority of the methylene blue elution occurred in our drug release studies (at pH 7.4, 41% released by unmodified, 64% released by TMOD, and 91% released by DMOD). To compare the nanogel uptake at 2 hours across cell lines, we computed the relative uptake as the ratio of the 2- and 24-hour uptake (400 μg/ml dose). A two-way analysis of variance (ANOVA) revealed that formulation accounted for only 11.1% of the total variation in relative uptake (not significant), whereas the cell line identity explained 38.6% of the total variation in relative uptake (significant at the $P < 0.001$ level). Consistent with the dose-response study presented above, DMOD uptake by colon cancer cells was 12.4 times greater than that of unmodified nanogels. Tyramine modification did not significantly affect the extent of nanogel uptake by any cell line.

The rapid association and uptake of DMOD nanogels by colon cancer cells is particularly interesting, as it suggests that this particular surface modification could enhance specific drug delivery to target tumor cells. However, as these experiments were conducted in homogeneous, static cell cultures, we are unable to conclude whether this preference for colon tumor cells would translate to in vitro coculture or in vivo models.

Photothermal actuation and therapy

One advantageous therapeutic quality of DMOD nanogels was their ability to act as an intrinsic reducing agent and, subsequently, act as centers for gold nanoparticle precipitation. DMOD nanogels with the three highest degrees of modification (0.78:1 DMOD or greater) were able to reduce gold chloride successfully, forming nanogel-coated gold nanoparticles. Nanogels with lesser quantities of *N*,*N*-dimethylethylenediamine did not form gold nanoparticles. Analysis of the composite nanogels' absorbance spectrum (Fig. 6A) revealed that the conjugates absorb visible light strongly, with a maximum absorbance wavelength of 536 nm. In the transmission electron microscopy (TEM) images presented here (Fig. 6B), the gold nanoparticles are visible as dark circular regions within the nanogel bulk. Some, but not all, of the nanogels contained gold nanoparticles after the precipitation reaction.

DMOD nanogel–gold nanoparticle composites (3.1:1) were suspended at various concentrations in 1× PBS and were irradiated with a 532-nm laser at 200 mW. Within 30 s, the PBS suspension reached an equilibrium temperature (Fig. 6C), while the heat rapidly dissipated when the laser was turned off. Nanogels alone, in the absence of precipitated gold nanoparticles, did not heat the surrounding medium when irradiated with the same laser, indicating that the gold nanomaterials were acting as a transducing element. The heat generated by laser irradiation increased with nanoparticle concentration, with a maximum heating of 10.3° ± 0.20°C by a nanoparticle-in-nanogel suspension (1 mg/ml) (Fig. 6D).

Surface coverage and activity of conjugated polypeptides

Next, we demonstrated the feasibility of peptide and protein coupling to the base nanogel platform. Peptides can be used to impart specific biological behaviors, including molecular recognition, cell targeting, cell penetration, and endosomal escape. Bioactive proteins can contribute enzymatic activity to the otherwise inert network or be used as a molecular recognition unit for targeting applications.

Two independent peptide conjugation reactions were explored: one for coupling cysteine-containing peptides via a thiol-maleimide reaction and a second for coupling the N-terminal amine or pendant lysine groups to carboxylic acids in the nanogel network. Five diverse, cysteine-containing peptide sequences were selected to sample a diverse array of peptide properties (two cationic, two anionic, and one electrically neutral at physiological pH, all water soluble). These peptides were previously identified by the authors as candidates for trypsin recognition in physiological fluids. In the present study, they were used as model oligopeptides to optimize a generalized nanogel-peptide conjugation strategy and conclude relationships between a peptide's formal charge and its coupling efficiency. In a two-step conjugation schema (Fig. 7A), we first coupled a maleimide-terminated linker molecule to the nanogels via carbodiimide-mediated coupling (pH 4.5). After 2 hours, we adjusted the nanogel suspension pH to 7.0 to favor the thiol-maleimide click reaction with the cysteine-containing peptides, as opposed to any amine–carboxylic acid side reaction (i.e., those between the nanogels' carboxylic acid and the peptides' N terminus, or peptide dimerization via the C and N termini of multiple peptides).

We were successful in conjugating all five peptides to the network, demonstrating the feasibility of conjugating diverse peptide ligands to the platform. Peptide content, within each nanogel network, was quantified with a Micro BCA colorimetric assay. Cationic (FAHWWC and HAHWEC) and electrically neutral (CDHFAI) peptides were incorporated with nearly complete efficiency (theoretically complete

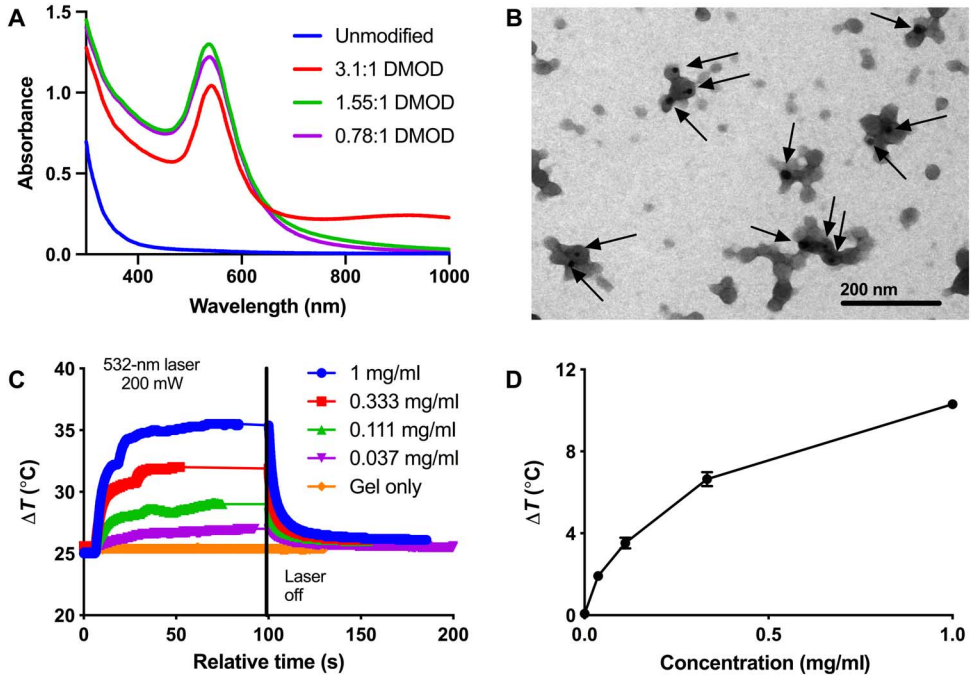

Fig. 6. Gold nanoparticle precipitation and photothermal therapy. Gold nanoparticles were precipitated in DMOD nanogels. DMOD gels with a 0.39:1 ratio of *N*,*N*-dimethylethylenediamine:methacrylic acid or less were unable to facilitate gold nanomaterial formation. (**A**) Absorbance spectra of composite nanogels containing gold nanoparticles. (**B**) Transmission electron micrographs of gold nanomaterials within 3.1:1 DMOD nanogels. Arrows point to gold nanoparticles. (**C**) Proof of concept for the composite nanogels' ability to transduce visible light (λ = 532 nm) into heat. DMOD (3.1:1) nanogels with gold nanoparticles effectively and rapidly heated a 1× PBS suspension. (**D**) Concentration-dependent photothermal activity of 3.1:1 DMOD–gold nanoparticle composites (n = 4, mean ± SD).

incorporation was 2% of the dry weight). On the other hand, anionic peptides were incorporated with lesser efficiency (43.7 ± 8.5% and 50.9 ± 8.6% for CDNWQY and ADCFLQ, respectively) (Fig. 7C). This highlighted the effect of peptide formal charge, which influences its equilibrium partitioning in the nanogel phase during the conjugation reaction, on efficient coupling. The extent of nanogel decoration with anionic peptides was increased by elevating the concentration of the anionic peptide in the coupling reaction, but is still significantly less efficient than the coupling of neutral and cationic peptides. Nanogel decoration with peptide, at 2 wt %, did not significantly alter the nanogels' size or zeta potential (Fig. 7D).

In a separate bioconjugation schema, the peptides were linked directly to the nanogel network via a reaction between the peptide N terminus and pendant carboxylic acid groups (Fig. 7B). Again, conjugation of a cationic peptide (HAHWEC) was efficient, as the quantity of the peptide within the network was readily controlled by modulating the peptide concentration in the coupling reaction (Fig. 7E). Our model anionic peptide (CDNWQY) was incorporated into the nanogels, but with a lesser efficiency (62.7 ± 15.0%, depending on the peptide concentration in the modification solution).

Wheat germ agglutinin (WGA) and horseradish peroxidase (HRP) were conjugated to nanogels via carbodiimide-mediated coupling, with 2 wt % protein in the modification reaction. These model proteins were selected, as they are commonly applied for immunohistochemistry and biosensing applications, respectively. As a result of selecting these two protein targets, we had methods for verifying the retention of protein activity following conjugation to the nanogels. Furthermore, the result is applicable to other proteins that have affinity for extracellular targets (similar to WGA) or catalyze small-molecule conversion (similar to HRP). Each protein was incorporated successfully (Fig. 7F) and retained its bioactivity after conjugation. HRP activity was quantified by the colorimetric determination of enzymatic conversion of 3,3′,5,5′-tetramethylbenzidine (TMB) substrate. Standard curves were generated for TMB conversion as a function of HRP concentration (free HRP or HRP bound covalently to nanogels). By comparing the conjugated HRP activity to that of free HRP at the same concentration, we determined that 66.5 ± 33% of the HRP activity was conserved (Fig. 7G). This provided evidence that our nanogels acted as scaffolds for retaining and presenting bioactive HRP to the surrounding environment.

WGA activity was assessed by determining the effectiveness with which WGA-labeled nanogels labeled fibroblast cell membranes. Fibroblasts were selected because unlabeled nanogels neither associate with fibroblast cell membranes nor are uptaken by fibroblasts within 2 hours, as quantified in Fig. 6 and illustrated in fig. S10. Therefore, colocalization of nanogels with the fibroblast membranes, or uptake into the cytosol, is due to the membrane-targeting activity of WGA. As shown in Fig. 7H, the WGA-labeled nanogels (red) colocalize with the cell cytosol, indicating that the conjugated WGA facilitated cell-nanogel interactions and subsequent uptake.

DISCUSSION

Here, we documented a modular, tunable nanogel platform for therapeutic applications. P(AAm-co-MAA) nanogels were decorated with numerous amine-containing ligands (i.e., small molecules, peptides, and proteins) and retained the ligand bioactivity (i.e., intrinsic reducing ability, pH sensitivity, hydrophobicity, molecular recognition characteristics, and enzymatic activity). We tuned the extent of ligand decoration by modulating the characteristics of the modification reaction and yielded a range of therapeutic capabilities, including cell targeting,

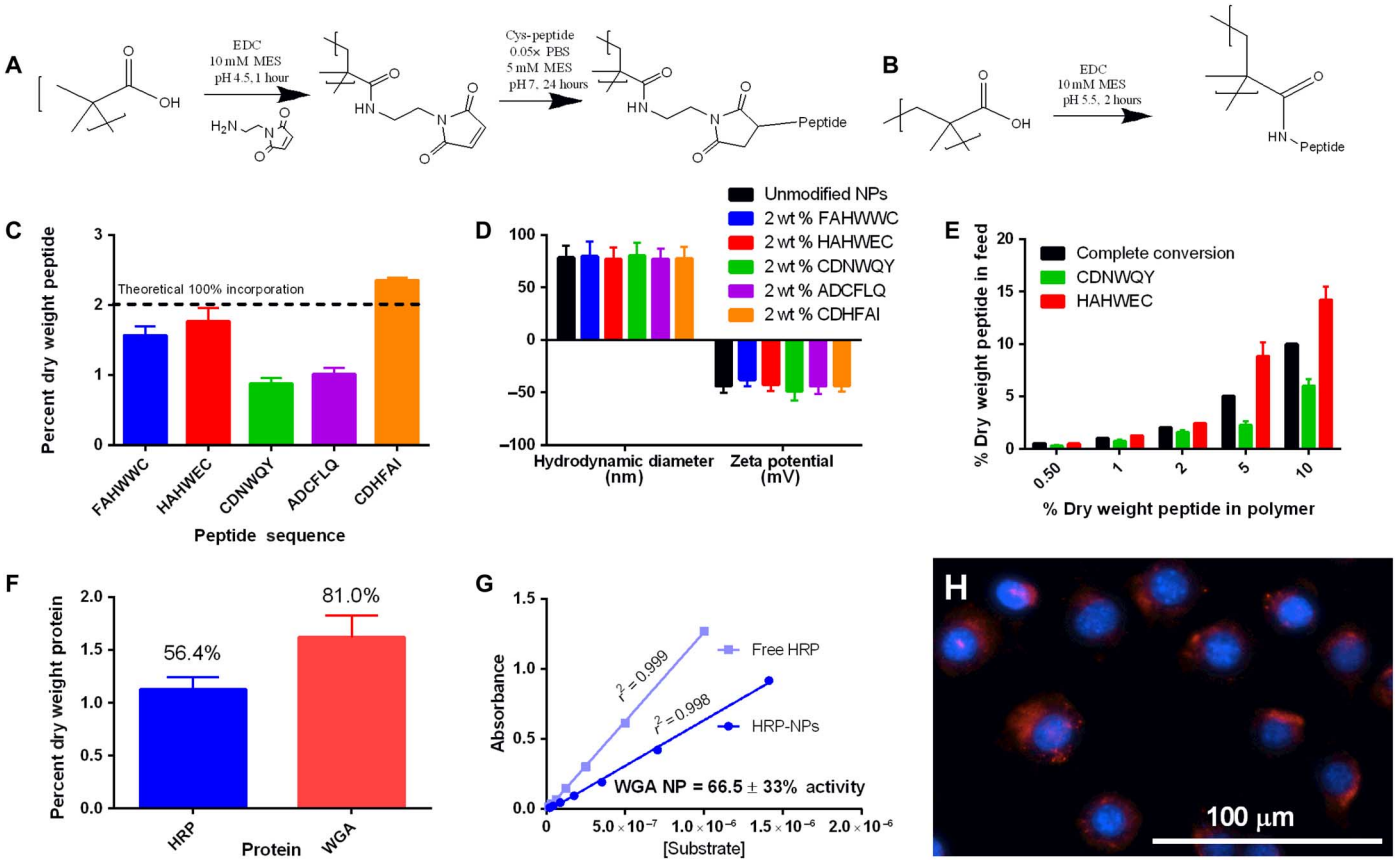

Fig. 7. Coupling efficiency and bioactivity of peptide and protein-nanogel conjugates. (**A**) A thiol-maleimide click reaction effectively conjugated cysteine-containing peptides to the nanogel network. (**B**) A carboxylic acid–amine reaction linked the peptides' N terminus with the carboxylic acid–containing nanogels. (**C**) Differential incorporation of diverse peptides was explained by their net charge at physiological pH. (**D**) Nanogel conjugation at 2 wt % did not significantly alter the nanogel diameter or zeta potential. (**E**) Peptide content in the final conjugate product can be readily tuned by altering the peptide feed concentration via reaction scheme (B). (**F**) Horseradish peroxidase (HRP) and wheat germ agglutinin (WGA) were incorporated into nanogels with 56.4 and 81% efficiency, respectively. (**G**) HRP retained 66.5 ± 33% of its activity upon conjugation to the nanogel platform, as evidenced by the ability of HRP-nanogel conjugates to convert TMB substrate. (**H**) WGA-NP conjugates retained native WGA activity, as they bound and stained the cell membrane of L929 murine fibroblasts (blue, DAPI stain of nucleus; red, WGA-NP conjugates) (C to F, n = 3, mean ± SD; G and H, n = 3, representative data).

enhanced nanomaterial uptake, intelligent drug delivery, and photothermal therapy.

In its present form, unmodified P(AAm-co-MAA) nanogels are suitable for loading high weight fractions of hydrophilic, cationic therapeutics. A suitable initial chemotherapeutic agent will be 5-fluorouracil, which is used to treat a number of cancers including colorectal cancer. These unmodified nanogels exhibited sustained therapeutic delivery for greater than 6 hours. Tyramine-modified nanogels were responsive to the pH environment and, as a result, delivered methylene blue more rapidly in acidic than neutral buffer. *N*,*N*-dimethylethylenediamine–modified nanogels were amphoteric in nature, eluted methylene blue the most rapidly of the tested formulations, and increased nanogel uptake by colon cancer cells.

Gold nanoparticle precipiation enabled photothermal therapy. Following DMOD nanogel accumulation in tumor sites, excitation with a focused green laser would heat the tumor tissue. Previous studies using gold nanoparticles for photothermal therapy applications have demonstrated efficacious heating using green light (*28*, *29*). However, our platform combines photothermal therapy and chemotherapeutic delivery in a new, modular manner. In the future, platform functionalization with targeting peptides, monoclonal antibodies, or other targeting molecules could further enhance nanogel targeting and cell uptake.

As presented in Introduction, research on treating cancer with multiple therapeutic modalities is increasing in prevalence (*30*, *31*). This platform technology, with its highly tunable nature, is amenable to delivering multiple chemotherapeutics and facilitating combination therapies, each with precise targeting or environmental responsiveness. Calibrated combinations of modified and unmodified nanogels in a single regimen could produce new physical distributions and release profiles of therapeutic agents in the future.

In addition to demonstrating the use of a new platform technology, we introduced multiple new characterization methods, which will be of utmost use to researchers developing nanoscale devices for precision medicine. In particular, while QCM methods have been used previously to study the deposition of nanomaterials on solid surfaces or the interfacial interactions governing monolayer self-assembly (*32*–*34*), the use of QCM to study swelling and biodegradation of nanogel materials is novel. Similarly, while nanomaterial internalization by cells has been an active area of research, using methods such as confocal microscopy and flow cytometry (*35*, *36*), we developed a high-throughput microplate assay for nanogel uptake. As a direct result of having this new analysis

tool, we were able to screen the dose-dependent and kinetic uptake of our modified nanogels by three relevant cell lines.

In conclusion, we engineered a new nanogel platform, which is modularly tunable for precision medicine applications. We quantified the extent to which nanogel composition altered drug-material interactions for the loading and release of cargo, transduction of external signals, targeting of proteins, and uptake by cells. Our new methods, described herein, will also provide new tools to the drug delivery field to rapidly screen or precisely quantify biological interactions with engineered nanomaterials in the future.

MATERIALS AND METHODS

Synthesis of P(AAm-co-MAA) nanogels

Nanogels were synthesized by inverse emulsion polymerization, as previously optimized by Zhong *et al.* (*16*). Acrylamide [75 mole percent (mol %)], methacrylic acid (22.5 mol %), and methylene bisacrylamide (2.5 mol %) were dissolved in water at 42 wt %. This aqueous phase (2.762 ml) and *N*,*N*,*N*′,*N*′-tetramethylethylenediamine (50 μl; catalyst) were added slowly to a stirring solution of Brij 30 (151.4 mM) and AOT (dioctyl sulfosuccinate sodium salt; 30.3 mM) in hexanes (50 ml) to form a water-in-oil emulsion. This prepolymer emulsion was purged with nitrogen for 20 min to remove dissolved oxygen, and polymerization was initiated by injecting 10 mg of nitrogen-purged ammonium persulfate [100 μl of a freshly prepared stock (100 mg/ml) in ultrapure water]. After 2 hours, the reaction was stopped by opening the round-bottom flask to air, and the nanogels were purified by precipitation in ethanol (three times) followed by either ionomer collapse or dialysis against a water:ethanol gradient.

In ionomer collapse, the nanogels were suspended in 0.5 N sodium hydroxide and precipitated with the addition of a threefold volume excess of acetone. Precipitated nanogels were collected by centrifugation (3200*g* for 5 min), and the collapse procedure was repeated an additional four times. In gradient dialysis, nanogels were suspended in a 50:50 water:ethanol mixture and dialyzed against a decreasing water:ethanol gradient for >5 days with twice-daily dialysate change. Nanogels purified by both ionomer collapse and gradient dialysis were then exchanged into ultrapure water by dialysis. All purified nanogels were lyophilized and stored at room temperature.

For studies involving degradable nanogels, synthesis was conducted in the manner described above, with *N*,*N*′-bis(acryloyl)cystamine substituted for methylene bisacrylamide. *N*,*N*′-bis(acryloyl)cystamine is a biodegradable cross-linker that is labile via reduction of its disulfide bond. Cross-linker comprised 2.5 mol % of the monomer feed, and the masses of acrylamide and methacrylic acid were adjusted such that total monomer concentration remained 42 wt % in water.

Quantification of biodegradation using DLS

Nanogels were suspended at 10 mg/ml in 1× PBS and adjusted to pH 7.4. Then, 0.5 ml of nanogels and 0.5 ml of DTT or glutathione (20 mM in 1× PBS, pH 7.4) were mixed in a polystyrene cuvette, immediately after which light scattering measurements were recorded. Measurements were recorded using a Zetasizer Nano ZS (Malvern) with a manual attenuation (Attn, 7), measurement position (4.65 mm), and measurement time (10 s). Measurements were taken repeatedly for 50 min. In each interval, a hydrodynamic diameter and count rate were recorded. Because count rate trends with the number of particles in solution (*37*), the count rate at a given time, normalized to the initial count rate, provided a measure of the degree of degradation.

Quantification of biodegradation using QCM

QCM studies were conducted using QSense E4 QCM-D (Biolin Scientific). Uncoated gold sensors were washed in a 5:1:1 volume ratio of ultrapure water, ammonia hydroxide (25 volume %), and hydrogen peroxide (30 volume %) at 75°C for 5 min. The sensors were then washed with an excess of water and an excess of ethanol and were dried under nitrogen. Immediately prior to experimentation, clean sensors were treated with ultraviolet/ozone for 10 min.

All experiments were conducted in their entirety at 37°C and a flow rate of 0.200 ml/min. A stable baseline for the sensors was achieved by flowing 1× PBS for at least 10 min. Then, the sensors were coated with an amine-terminated monolayer through the addition of cysteamine HCl (10 mg/ml in 1× PBS). Nanogels activated with 1-ethyl-3-(3-dimethylaminopropyl)carbodiimide (EDC) (twofold molar excess relative to MAA) were flowed over the modified sensor at 2 mg/ml. After a stable coating was obtained (as evidenced by no further fluctuation in the frequency or dissipation), 1× PBS was flowed over the sensor to wash away unreacted polymer and remaining catalyst. The change in resonance frequency, as a result of nanogel coupling, was recorded as a measure of the bound nanogel mass.

Nanogels were swelled in a series of buffers differing in ionic strength (PBS buffers at pH 7.4 diluted to 5×, 2×, 1×, 0.5×, 0.1×, and 0.01× with ultrapure water) as well as 1× PBS buffer adjusted to different pH values (3, 5, 7, 9, and 11). The purpose of these swelling steps was twofold: to quantify the responsiveness of nanogels to environmental conditions and to verify that the nanogels are behaving as expected despite their immobilization. The frequency and dissipation values were monitored to quantify the nanogels' water uptake or expulsion in each buffer condition, as well as to determine the viscoelastic properties of the nanogel layer.

Nanogels were degraded by flowing a 10 mM DTT solution over the nanogel-modified sensors. The frequency and dissipation values were monitored to determine the mass loss during degradation as well as probe changes in viscoelastic properties that indicate the degradation mechanism (i.e., bulk degradation or surface erosion). In each case, the mass immobilized or adsorbed was quantified by the Sauerbrey equation

$$\Delta m = -C\,\frac{\Delta f}{n}$$

where m is the mass adsorbed or immobilized, C is a constant that depends on the intrinsic properties of quartz [for a 5-MHz crystal, $C = 17.7$ ng/(cm^2 Hz)], and n is the overtone number (i.e., 3 and 5). The relative mass was computed by normalizing the change in mass, due to swelling or degradation, to the mass of nanoparticles immobilized (*32*, *38*). It is also equal to the ratio of the frequency changes

$$\frac{\Delta m_{\text{degradation}}}{\Delta m_{\text{immobilized}}} = \frac{\Delta f_{\text{degradation}}}{\Delta f_{\text{immobilized}}}$$

Modification of P(AAm-co-MAA) with bioactive small molecules

Purified, dried nanogels were suspended in 10 mM MES buffer and adjusted to pH 4.5 ± 0.05. Tyramine or *N*,*N*-dimethylethylenediamine was dissolved in water at 25 mg/ml. EDC hydrochloride was dissolved immediately prior to use in MES buffer at 56 mg/ml. Each reaction was composed of 5 ml of nanogels (50 mg), 1 ml of EDC solution (56 mg of EDC, a 2:1 molar ratio EDC:MAA by original synthesis feed, and 0.8:1

molar ratio EDC:acid subunit when confirmed by titration analysis), and a variable volume of tyramine or *N*,*N*-dimethylethylenediamine (1.6 ml for the highest degree of modification and cut by half for each subsequent reaction). The highest modification ratio (by moles) tested was 2:1 tyramine:MAA and a 3.1:1 *N*,*N*-dimethylethylenediamine:MAA. In each "highest modification" case, the ligand concentration was 80% that of the nanogels by mass. As a control, nanogels were subjected to the reaction conditions (MES buffer, pH 4.5, 56 mg of EDC) in the absence of ligand. Modified nanogels were purified by dialysis against ultrapure water (>72 hours, frequent water changes). Reactions were completed in duplicate.

FTIR spectroscopy, DLS, and zeta potential measurement

The physicochemical properties of nanogels were quantified by attenuated total reflectance–FTIR spectroscopy (Nicolet iS10 FTIR Spectrometer; Thermo Fisher Scientific), DLS, and zeta potential measurement (Zetasizer Nano ZS; Malvern). Dried nanogels were pressed in contact with a germanium crystal, and the IR absorption spectrum was recorded from 4000 to 675 cm^{-1}. All presented spectra are the average of 64 measurements. All spectra were normalized such that the magnitude of their largest peak was 1 U, and their baseline was set at zero. All DLS measurements, unless otherwise stated, were obtained at a nanogel concentration of 2 mg/ml in 1× PBS, adjusted to pH 7.4. All zeta potential measurements, unless otherwise stated, were taken at a nanogel concentration of 2 mg/ml in 5 mM sodium phosphate buffer, adjusted to pH 7.4.

Quantitative potentiometric titration

The extent of modification with tyramine, *N*,*N*-dimethylethylenediamine, or 5-(aminoacetamido)fluorescein was quantified by potentiometric titration. Ten milligrams of modified or unmodified nanogels was suspended in 60 ml of 5 mM potassium chloride buffer. The suspension was adjusted to pH 10 with 1 N sodium hydroxide to completely deprotonate pendant methacrylic acid groups. The solution was titrated through the equivalence point with 0.01 N hydrochloric acid (HCl) using an autotitrator (Hanna HI901C). We titrated the nanogel suspensions from a basic-to-acidic environment to ensure that the nanogels were swollen during the entirety of adjustment to equivalence. The equivalence point for methacrylic acid–containing nanogels was consistently at pH 4.8.

We assume that at equivalence (pH 4.8), exactly half of the acid moieties are protonated. We also assume that at a pH three points above equivalence (pH 7.8), 0.1% of the acid groups are protonated. The volume of 0.01 N HCl needed to adjust pure 5 mM KCl buffer from pH 7.8 to pH 4.8, as well as the volume needed to adjust each nanogel suspension the same increment, was recorded. Using these measurements and the stated assumptions, we calculated the mass fraction of methacrylic acid groups using

$$\frac{m_{\mathrm{MAA}}}{m_{\mathrm{nanogels}}} = \left(\frac{1}{0.499}\right)(V_{\mathrm{suspension}} - V_{\mathrm{buffer}}) \times N_{\mathrm{titrant}} \times \mathrm{MW}_{\mathrm{MAA}} \times \frac{1}{m_{\mathrm{nanogels}}}$$

where m_{nanogels} was 0.010 g, N_{titrant} was 0.01 M, the molecular weight of methacrylic acid ($\mathrm{MW}_{\mathrm{MAA}}$) is 86.06 g/mol, and both volumes were measured in liters.

The extent of nanogel functionalization with peptides or proteins was quantified using a Micro BCA colorimetric assay (Thermo Fisher Scientific), as described previously (*39*). Modified or unmodified nanogels, suspended at 2 mg/ml in 1× PBS (pH 7.4 ± 0.05), were combined at an equal volume ratio with Micro BCA working reagent and mixed for 2 hours at 37°C (constant mixing). The absorbance of the reduced supernatant (λ = 562 nm) was used to quantify the suspension's peptide concentration, relative to standard curves generated for each pure peptide or protein. The background absorbance of unmodified nanogels under the same testing conditions was subtracted from each measurement.

Cell culture

L929 murine fibroblasts, RAW 264.7 murine macrophages, and SW-48 human colorectal epithelial carcinoma cells were chosen as model cells to properly assess nanomaterial interactions with model connective, immune, and epithelial tissues that would interact in vivo. All cells were cultured in T-75 tissue culture–treated flasks and were used at passages ranging from 6 to 20.

Cells were incubated in a sterile 37°C, 5% CO_2 environment. Culture medium for all three cell lines was phenol red–containing high-glucose Dulbecco's modified Eagle's medium (DMEM), supplemented with 10% fetal bovine serum (FBS), 2 mM L-glutamine, and 1% penicillin-streptomycin. Cells were passaged once they reached 80 to 90% confluency. Experiment medium for all three cell lines was phenol red–free, high-glucose DMEM with 2% FBS, 2 mM L-glutamine, and 1% penicillin-streptomycin. Experiments were conducted when cells reached 50 to 70% confluency.

For all cell assays, L929 and RAW 264.7 cells were seeded in tissue culture–treated 96-well plates at a density of 10,000 cells per well. SW-48 cells were seeded in similar plates at 25,000 cells per well. Cells were given a minimum of 24 hours to attach and reach 50 to 70% confluency before cytotoxicity, or nanogel uptake assays were performed.

Model drug loading and release

Methylene blue was selected as a model hydrophilic, cationic therapeutic. Methylene blue is a photosensitizer and was selected because of its similarity in hydrophilicity and ionization to hydrophilic chemotherapeutics (i.e., 5-fluorouracil), as well as its compatibility with our hydrophilic, anionic nanogels. Methylene blue was loaded into modified and/or unmodified nanogels by equilibrium partitioning in ultrapure water. For loading experiments, methylene blue (2 mg/ml) and purified nanogels (2 mg/ml) were mixed for 15 min in distilled water. Drug loading was quantified by removing a sample (500 μl) and separating the unbound drug by ultrafiltration (Sartorius Vivaspin 500; 300,000 MWCO). The unbound methylene blue was quantified by absorbance (λ = 590 nm) relative to a standard curve. Loaded or partitioned methylene blue was quantified using

$$Q = \frac{(C_0 - C_e)V}{m}$$

where Q is the mass ratio of loaded methylene blue to nanogels, C_0 is the methylene blue concentration in the loading solution (1 mg/ml), C_e is the unbound concentration of methylene blue (that passed through the filter), V is the volume of the loading solution, and m is the mass of nanogels in the loading solution.

Prior to drug release experiments, unloaded drug was removed by dialysis against ultrapure water (24 hours, 12,000 to 14,000 MWCO). Methylene blue–loaded nanogels [10 ml, nanogels (1 mg/ml), methylene blue (1 mg/ml) in the loading solution, variable methylene blue loaded], still within dialysis tubing, were transferred to 1× PBS solution

(400 ml) at pH 4.5 or 7.4 under constant stirring at $T = 37$°C. At regular time intervals (15 min, 30 min, 1 hour, 1.5 hours, 2 hours, 4 hours, 8 hours, 24 hours, and 28 hours), samples were taken both from within and outside the dialysis tubing. For samples drawn from within the dialysis tubing, loaded and released methylene blue were separated by ultrafiltration. The dialysate was exchanged for fresh buffer at the 2-hour time point and each time point thereafter to simulate drug metabolism. This dialysate exchange ensured that a concentration gradient (between the nanogel and solution phases) was maintained to facilitate complete methylene blue elution. The total released drug was quantified for the first time point as

$$m_{\text{released}} = V_{\text{within tubing}} C_{\text{MB,within tubing}} + V_{\text{dialysate}} C_{\text{MB,dialysate}}$$

where the volume parameters describe the total volume within and outside of the dialysis tubing, respectively, and the concentration parameters capture the released methylene blue present in each solution location.

Note that the volume within the dialysis tubing changes with each time point (as sample is depleted) and that released methylene blue within the dialysis tubing eventually dissipates into the dialysate. It is important to correct for these mathematically. For example, at the 30-min time point, the methylene blue released in the 15-min increment from 15 to 30 min was calculated using

$$\begin{aligned} m_{\text{released}} = {} & (V_{\text{within tubing}} C_{\text{MB,within tubing}})_{t=30} - \\ & (V_{\text{within tubing}} C_{\text{MB,within tubing}})_{t=15} + \\ & (V_{\text{dialysate}} C_{\text{MB,dialysate}})_{t=30} - (V_{\text{dialysate}} C_{\text{MB,dialysate}})_{t=15} \end{aligned}$$

Please note that this equation holds for all future time points as well, changing the respective time indicators, with the one exception that the final term is omitted if the dialysate buffer was exchanged prior to the interval.

Cytotoxicity

Culture medium was removed by plate inversion and replaced with experiment medium containing hydrogel microparticles (0.0005 to 2 mg/ml). In the case of degraded nanogels, the culture medium containing degradable nanogels was spiked with 10 mM glutathione and incubated at 37°C for 24 hours prior to the experiment.

Plate layouts were pseudorandomized. To pseudorandomize, we distributed the samples and controls throughout each microplate to ensure that each sample/control was positioned equitably along the plate exterior or within the interior. This controlled for variation in cell proliferation explained by well location within the plate. Following 24-hour incubation, cytotoxicity was quantified via metabolic activity (MTS) and cell membrane integrity (LDH assay).

For MTS assays, the nanogel-containing experiment medium was removed by plate inversion, and cells were washed with 37°C Dulbecco's PBS (DPBS) twice to remove adsorbed nanogels and cell debris. Then, 100 μl of MTS assay buffer (MTS diluted 1:6 in experiment medium) was added to each well, and relative metabolic activity of each cell sample was quantified by measuring the MTS metabolism (90 min at 37°C) within each well, relative to control, as specified by the manufacturer (Promega).

For LDH assays, LDH assay buffer (100 μl) was added directly to the cell media containing nanogels and any cell debris. The relative membrane integrity was calculated by measuring the LDH activity (excitation, 560 nm; emission, 590 nm) according to the following relation

$$\text{Relative membrane integrity} = 100 - 100 \times \frac{\text{sample} - \text{blank}}{\text{max release} - \text{blank}}$$

where the sample measurement is the fluorescence of the treatment media with LDH assay buffer, the blank is the cell culture medium and assay buffer without cells, and the max release is the LDH buffer and treatment media after a 20 min incubation of cells with media and 2 μl of lysis buffer (Promega).

Nanogel uptake

A high-throughput fluorescence imaging assay was developed for rapidly screening cells' uptake of modified and unmodified nanogels. Fluorescently tagged nanogels, with the addition or lack of tyramine or *N*,*N*-dimethylethylenediamine, were suspended in phenol red–free DMEM at concentrations ranging from 1000 to 6.25 μg/ml. Cells were dosed with either a gradient of nanogel concentration (24-hour incubation) or a set concentration for a range of time (concentration of 400 μg/ml).

For concentration-dependent nanogel uptake assays, culture medium was removed from each well by plate inversion and replaced by treatment medium containing suspended nanogels. Cells were allowed to incubate for 24 hours in the presence of nanogels (100 μl per well). Following incubation, the nanogels were removed by aspiration, followed by three washes with cold DPBS. Cells were fixed with cold paraformaldehyde solution for 10 min (50 μl per well).

For time-dependent nanogel uptake assays, culture medium was removed from each well and replaced with treatment media containing nanogels (400 μg/ml) by aspiration in an inverse time manner (i.e., 24-hour time point first, 15-min time point last) (100 μl per well). This was scheduled in such a way that all wells reached their end point simultaneously. Nanogel suspensions were removed from the cells by aspiration, and the cells were washed three times with cold DPBS (100 μl per well). These cells were also fixed with cold paraformaldehyde solution (50 μl per well).

Cells were stained directly in the microplates for fluorescence imaging. Following fixation, each well was washed three times with cold Hanks' balanced salt solution (HBSS) (100 μl per well). Then, the cell membranes were stained with a WGA Alexa Fluor 594 conjugate solution (3 μg/ml) in cold HBSS (15 min) (50 μl per well). After three more washes with cold HBSS (100 μl per well), the cells were stained with a DAPI solution (1 μg/ml) in cold HBSS for 10 min (50 μl per well). Each well was washed three times with cold HBSS prior to imaging (100 μl per well). Imaging was conducted with 100 μl of fresh HBSS in each well.

Cell imaging was conducted at high throughput using a Cytation 3 plate reader (BioTek) with Gen5 software (version 3.04) equipped with DAPI, GFP, and Texas Red filters (DAPI: excitation, 377 nm; emission, 447 nm; Texas Red: excitation, 586 nm; emission, 647 nm; and GFP: excitation, 469 nm; emission, 525 nm) and an Olympus 20× objective. Imaging parameters were optimized to the most fluorescent samples to prevent saturation and were held constant to enable both qualitative and quantitative image analyses between cell lines and treatments [DAPI: light-emitting diode (LED) intensity, 5; integration time, 63; and gain, 0; Texas Red: LED intensity, 10; integration time, 100; and gain, 13.8; and GFP: LED intensity, 10; integration time, 158; and gain, 15].

Four images were taken for each well, and images were preprocessed with a background subtraction step prior to qualitative analysis.

For quantitative analysis, the fluorescence of the whole well was taken for each relevant channel (DAPI, Texas Red, and GFP with gain values of 60, 100, and 120, respectively). To normalize the nanoparticle signal intensity to the cell count, we normalized the fluorescence intensity of GFP to the DAPI channel. The relative nanogel uptake for each cell line–condition pair is given as this ratio.

Analysis of photothermal therapy

To precipitate gold nanoparticles within the hydrogel nanogels, chloroauric acid (0.05 wt %) and nanogels (1 mg/ml) were suspended in ultrapure water and mixed (Eppendorf ThermoMixer) at 1000 rpm and 60°C for 1 hour. Nanogels with precipitated nanoparticles were used in further experiments without purification. These composite nanogels were characterized by their visible absorption spectra (300 to 1000 nm in 1-nm intervals using a Cytation 3 microplate reader) as well as by TEM (FEI Tecnai Transmission Electron Microscope, operating at 80 kV, cast on carbon-coated grid, and stained with uranyl acetate).

Photothermal experiments were conducted as previously described (*40*, *41*). For photothermal therapy experiments, a 532-nm laser diode (PN156-10.07-0447) was used. This laser wavelength was within the maximum absorbance peak of the gold nanoparticle–containing nanogels. The nanogels were suspended in ultrapure water at 1 mg/ml, and 1 ml of each nanogel suspension was added to a 24-well microplate. The laser, operated at a power of 200 mW, was focused on a circular area with a 6-mm diameter using a convex lens (Thorlabs Inc.), which was mounted at a 30° angle. Dynamic fluctuation in temperature, within the circular area, was measured using an indium antimonide IR camera (FLIR Systems Inc.).

Modification of P(AAm-co-MAA) with peptides or proteins

For peptide modification through a thiol-maleimide click reaction, the nanogels were first modified with *N*-(2-aminoethyl)maleimide. Purified, dried nanogels were suspended in 10 mM MES at 10 mg/ml and adjusted to pH 4.5. Carboxylic acids were first activated by the addition of a twofold molar excess EDC (relative to MAA content), after which the *N*-(2-aminoethyl)maleimide trifluoroacetate salt was added. The amount of this linker molecule added was calculated such that if 100% peptide coupling were achieved, then the final peptide concentration would be 2 wt % of the dry nanogel. During this modification reaction, the pH was carefully maintained at 4.5. After 30 min, the pH of the solution was raised to 7.0 with 1 N sodium hydroxide (to terminate the carboxylic acid–amine reaction), and the thiol-containing hexamer peptides (FAHWWC, HAHWEC, CDNWQY, ADCFLQ, and CDHFAI) were dissolved in 0.1× PBS at 10 mg/ml, adjusted to pH 7, and added (final peptide concentration of 2 wt % relative to the nanogels). This thiol-maleimide reaction was allowed to proceed overnight at room temperature under constant mixing. The nanogels were purified by dialysis against ultrapure water (12,000 to 14,000 MWCO, >72 hours, frequent water changes).

For peptide modification through a carboxylic acid–amine reaction, the nanogels were suspended in 10 mM MES, and pH was adjusted to 5.5. Carboxylic acids were activated with a twofold molar excess (relative to MAA) of EDC. Peptides were dissolved in 10 mM MES at 10 mg/ml and adjusted to pH 5.5. The proper volume of the peptide solution was added to each modification reaction to achieve the desired extent of peptide decoration (i.e., 0 to 10 wt %, relative to the dried nanogels). Nanogels were purified by dialysis against ultrapure water.

Nanogel modification with bioactive proteins was conducted in the same manner as the peptide carboxylic acid–amine coupling, except for that WGA Alexa Fluor 594 (Thermo Fisher Scientific) or HRP (Worthington) was dissolved at 1 mg/ml in 10 mM MES and added to the modification reaction at a final protein concentration of 2 wt % (relative to the dried nanogels).

Measurement of protein bioactivity

HRP bioactivity within modified nanogels was quantified by its ability to convert TMB substrate, relative to free HRP. Nanogels were dissolved at 2 mg/ml in 1× PBS (pH 7.4 ± 0.05) and diluted 1:8000 for a final concentration of 0.25 μg/ml. Lyophilized HRP (Worthington) was also dissolved at 2 mg/ml in 1× PBS and diluted 1:1,000,000 for a final concentration of 0.002 μg/ml. A calibration curve for HRP activity was generated via serial dilution with a maximum concentration of 0.002 μg/ml. In a 96-well microplate, 100 μl of HRP solution or nanogel suspension was mixed with 100 μl of TMB substrate solution (Pierce). After 10 min of incubation at ambient conditions, the reaction was stopped by adding 50 μl of 1 N sulfuric acid. The reaction product was quantified by visible absorbance at λ = 450 nm.

WGA bioactivity was quantified by its ability to recognize fibroblast cell membrane (via interaction with sialic acid and *N*-acetylglucosaminyl residues in the membrane). Fibroblasts were seeded in 96-well microplates at 10,000 cells per well and allowed to attach overnight. Cells were incubated in phenol red-free DMEM, supplemented with 2% FBS, containing WGA-conjugated nanogels at 1 mg/ml for 2 hours. As control samples, separate wells were incubated in media alone or media with unmodified nanogels (1 mg/ml) (2 hours). All wells were washed three times with cold DPBS and fixed with cold paraformaldehyde (IC Fixation Buffer; Invitrogen) for 10 min (50 μl per well).

After fixation, the nuclei of all cells were stained with DAPI (1 μg/ml in cold HBSS, 10 min). The plasma membranes of positive control cells were stained with WGA–Alexa Fluor 594 (3 μg/ml in cold HBSS, 15 min). After each staining step, all wells were washed three times with cold HBSS (100 μl per well).

Fibroblasts were imaged using the fluorescence imaging capabilities of the Cytation 3 microplate reader, equipped with a 20× Olympus objective. So that images could be compared qualitatively, common imaging parameters were used for all images [DAPI (nucleus): LED intensity, 5; integration time, 50; and gain, 0; Texas Red (WGA-nanogels and membrane stain): LED intensity, 10; integration time, 130; gain, 13.6]. Images were processed using Gen5 software (version 3.04), where the background fluorescence was subtracted from each image.

SUPPLEMENTARY MATERIALS

Supplementary material for this article is available at http://advances.sciencemag.org/cgi/content/full/5/9/eaax7946/DC1

Fig. S1. Proof of similarity for degradable and nondegradable P(AAm-co-MAA) nanogels.
Fig. S2. Nanogel swelling and degradation analysis with QCM.
Fig. S3. FTIR analysis of *N*,*N*-dimethylethylenediamine– or tyramine-conjugated nanogels.
Fig. S4. Potentiometric titration analysis of DMOD and TMOD nanogels.
Fig. S5. Full data of pH-responsive, modified nanogel swelling, including data for aggregated nanogels.
Fig. S6. Methylene blue loading in DMOD and TMOD nanogels.
Fig. S7. Nanogel cytotoxicity to murine fibroblasts, as determined by MTS and LDH assays.
Fig. S8. Cytotoxicity of degradable, nondegradable, and degraded nanogels to fibroblasts, macrophages, and colon epithelial cells.
Fig. S9. Cytotoxicity of fluorescent TMOD, DMOD, or unmodified (Fluor) nanogels.
Fig. S10. Representative images for dose-response and kinetic nanogel uptake.

REFERENCES AND NOTES

1. C. A. Mirkin, T. J. Meade, S. H. Petrosko, A. H. Stegh, *Nanotechnology-Based Precision Tools for the Detection and Treatment of Cancer* (Springer, 2015), vol. 166.
2. X. Xu, W. Ho, X. Zhang, N. Bertrand, O. Farokhzad, Cancer nanomedicine: From targeted delivery to combination therapy. *Trends Mol. Med.* **21**, 223–232 (2015).
3. A. Armiñán, M. Palomino-Schatzlein, C. Deladriere, J. J. Arroyo-Crespo, S. Vicente-Ruiz, M. J. Vicent, A. Pineda-Lucena, Metabolomics facilitates the discrimination of the specific anti-cancer effects of free-and polymer-conjugated doxorubicin in breast cancer models. *Biomaterials* **162**, 144–153 (2018).
4. W. B. Liechty, R. L. Scheuerle, J. E. Vela Ramirez, N. A. Peppas, Uptake and function of membrane-destabilizing cationic nanogels for intracellular drug delivery. *Bioeng. Transl. Med.* **4**, 17–29 (2018).
5. D. S. Spencer, A. S. Puranik, N. A. Peppas, Intelligent nanoparticles for advanced drug delivery in cancer treatment. *Curr. Opin. Chem. Eng.* **7**, 84–92 (2015).
6. R. Zhang, R. Xing, T. Jiao, K. Ma, C. Chen, G. Ma, X. Yan, Carrier-free, chemophotodynamic dual nanodrugs via self-assembly for synergistic antitumor therapy. *ACS Appl. Mater. Interfaces* **8**, 13262–13269 (2016).
7. F. Wang, J. Xiao, S. Chen, H. Sun, B. Yang, J. Jiang, X. Zhou, J. Du, Polymer vesicles: Modular platforms for cancer theranostics. *Adv. Mater.* **30**, 1705674 (2018).
8. A. M. Wagner, D. S. Spencer, N. A. Peppas, Advanced architectures in the design of responsive polymers for cancer nanomedicine. *J. Appl. Polym. Sci.* **135**, 46154 (2018).
9. Y. Luqmani, Mechanisms of drug resistance in cancer chemotherapy. *Med. Princ. Pract.* **14**, 35–48 (2005).
10. V. Malhotra, M. C. Perry, Classical chemotherapy: Mechanisms, toxicities and the therapeutc window. *Cancer Biol. Ther.* **2**, 1–3 (2003).
11. J. Kim, J. Kim, C. Jeong, W. J. Kim, Synergistic nanomedicine by combined gene and photothermal therapy. *Adv. Drug Deliv. Rev.* **98**, 99–112 (2016).
12. J. Conde, N. Oliva, Y. Zhang, N. Artzi, Local triple-combination therapy results in tumour regression and prevents recurrence in a colon cancer model. *Nat. Mater.* **15**, 1128–1138 (2016).
13. M. Liu, S. Shen, D. Wen, M. Li, T. Li, X. Chen, Z. Gu, R. Mo, Hierarchical nanoassemblies-assisted combinational delivery of cytotoxic protein and antibiotic for cancer treatment. *Nano Lett.* **18**, 2294–2303 (2018).
14. J. A. Kemp, M. S. Shim, C. Y. Heo, Y. J. Kwon, "Combo" nanomedicine: Co-delivery of multi-modal therapeutics for efficient, targeted, and safe cancer therapy. *Adv. Drug Deliv. Rev.* **98**, 3–18 (2016).
15. M. Bar-Zeev, Y. D. Livney, Y. G. Assaraf, Targeted nanomedicine for cancer therapeutics: Towards precision medicine overcoming drug resistance. *Drug Resist. Updat.* **31**, 15–30 (2017).
16. J. X. Zhong, J. R. Clegg, E. W. Ander, N. A. Peppas, Tunable poly (methacrylic acid-co-acrylamide) nanoparticles through inverse emulsion polymerization. *J. Biomed. Mater. Res. A* **106**, 1677–1686 (2018).
17. V. Biju, Chemical modifications and bioconjugate reactions of nanomaterials for sensing, imaging, drug delivery and therapy. *Chem. Soc. Rev.* **43**, 744–764 (2014).
18. S. Ahadian, R. B. Sadeghian, S. Salehi, S. Ostrovidov, M. Ramalingam, A. Khademhosseini, Bioconjugated hydrogels for tissue engineering and regenerative medicine. *Bioconjug. Chem.* **26**, 1984–2001 (2015).
19. J. R. Clegg, M. E. Wechsler, N. A. Peppas, Vision for functionally decorated and molecularly imprinted polymers in regenerative engineering. *Regen. Eng. Transl. Med.* **3**, 166–175 (2017).
20. E. Harrison, J. A. Coulter, D. Dixon, Gold nanoparticle surface functionalization: Mixed monolayer versus hetero bifunctional peg linker. *Nanomedicine* **11**, 851–865 (2016).
21. M. C. L. Giudice, F. Meder, E. Polo, S. S. Thomas, K. Alnahdi, S. Lara, K. A. Dawson, Constructing bifunctional nanoparticles for dual targeting: Improved grafting and surface recognition assessment of multiple ligand nanoparticles. *Nanoscale* **8**, 16969–16975 (2016).
22. J. Chen, S.-W. Huang, W.-H. Lin, R.-X. Zhuo, Tunable film degradation and sustained release of plasmid DNA from cleavable polycation/plasmid DNA multilayers under reductive conditions. *Small* **3**, 636–643 (2007).
23. Y. Zhan, M. Goncalves, P. Yi, D. Capelo, Y. Zhang, J. Rodrigues, C. Liu, H. Tomas, Y. Li, P. He, Thermo/redox/pH-triple sensitive poly (*N*-isopropylacrylamide-*co*-acrylic acid) nanogels for anticancer drug delivery. *J. Mater. Chem. B* **3**, 4221–4230 (2015).
24. H. Wutzel, F. H. Richter, Y. Li, S. S. Sheiko, H.-A. Klok, Poly [*N*-(2-hydroxypropyl) methacrylamide] nanogels by RAFT polymerization in inverse emulsion. *Polym. Chem.* **5**, 1711–1719 (2014).
25. P. A. Hassan, S. Rana, G. Verma, Making sense of Brownian motion: Colloid characterization by dynamic light scattering. *Langmuir* **31**, 3–12 (2014).
26. R. Guo, G. Yang, Z. Feng, Y. Zhu, P. Yang, H. Song, W. Wang, P. Huang, J. Zhang, Glutathione-induced amino-activatable micellar photosensitization platform for synergistic redox modulation and photodynamic therapy. *Biomater. Sci.* **6**, 1238–1249 (2018).
27. C. C. White, W. Clinton, R. A. Weiss, V. D. Bryan, "Unexpected" frequency behavior in QCM-D: When can frequency increase with increased adhered mass? *Soft Matter* **90**, (2018).
28. I. H. El-Sayed, X. Huang, M. A. El-Sayed, Selective laser photo-thermal therapy of epithelial carcinoma using anti-EGFR antibody conjugated gold nanoparticles. *Cancer Lett.* **239**, 129–135 (2006).
29. C. Ungureanu, R. Kroes, W. Petersen, T. A. M. Groothuis, F. Ungureanu, H. Janssen, F. W. B. van Leeuwen, R. P. H. Kooyman, S. Manohar, T. G. van Leeuwen, Light interactions with gold nanorods and cells: Implications for photothermal nanotherapeutics. *Nano Lett.* **11**, 1887–1894 (2011).
30. K. Habiba, J. Encarnacion-Rosado, K. Garcia-Pabon, J. C. Villalobos-Santos, V. I. Makarov, J. A. Avalos, B. R. Weiner, G. Morell, Improving cytotoxicity against cancer cells by chemo-photodynamic combined modalities using silver-graphene quantum dots nanocomposites. *Int. J. Nanomedicine* **11**, 107–119 (2016).
31. D. Jiang, Y. Sun, J. Li, Q. Li, M. Lv, B. Zhu, T. Tian, D. Cheng, J. Xia, L. Zhang, L. Wang, Q. Huang, J. Shi, C. Fan, Multiple-armed tetrahedral DNA nanostructures for tumor-targeting, dual-modality in vivo imaging. *ACS Appl. Mater. Interfaces* **8**, 4378–4384 (2016).
32. Q. Chen, S. Xu, Q. Liu, J. Masliyah, Z. Xu, QCM-D study of nanoparticle interactions. *Adv. Colloid Interf. Sci.* **233**, 94–114 (2016).
33. K. S. Siow, L. Britcher, S. Kumar, H. J. Griesser, QCM-D and XPS study of protein adsorption on plasma polymers with sulfonate and phosphonate surface groups. *Colloids Surf. B: Biointerfaces* **173**, 447–453 (2019).
34. M. Raudino, N. Giamblanco, C. Montis, D. Berti, G. Marletta, P. Baglioni, Probing the cleaning of polymeric coatings by nanostructured fluids: A QCM-D study. *Langmuir* **33**, 5675–5684 (2017).
35. A. R. Collins, B. Annangi, L. Rubio, R. Marcos, M. Dorn, C. Merker, I. Estrela-Lopis, M. R. Cimpan, M. Ibrahim, E. Cimpan, M. Ostermann, A. Sauter, N. El Yamani, S. Shaposhnikov, S. Chevillard, V. Paget, R. Grall, J. Delic, F. Goni-de-Cerio, B. Suarez-Merino, V. Fessard, K. N. Hogeveen, L. M. Fjellsbø, E. R. Pran, T. Brzicova, J. Topinka, M. J. Silva, P. E. Leite, A. R. Ribeiro, J. M. Granjeiro, R. Grafstrom, A. Prina-Mello, M. Dusinka, High throughput toxicity screening and intracellular detection of nanomaterials. *Wiley Interdiscip. Rev. Nanomed. Nanobiotechnol.* **9**, e1413 (2017).
36. B. B. Manshian, S. Munck, P. Agostinis, U. Himmelreich, S. J. Soenen, High content analysis at single cell level identifies different cellular responses dependent on nanomaterial concentrations. *Sci. Rep.* **5**, 13890 (2015).
37. W. B. Liechty, R. L. Scheuerle, J. E. V. Ramirez, N. A. Peppas, Cytoplasmic delivery of functional siRNA using pH-Responsive nanoscale hydrogels. *Int. J. Pharm.* **562**, 249–257 (2019).
38. B. D. Vogt, E. K. Lin, W.-l. Wu, C. C. White, Effect of film thickness on the validity of the Sauerbrey equation for hydrated polyelectrolyte films. *J. Phys. Chem. B* **108**, 12685–12690 (2004).
39. J. R. Clegg, J. X. Zhong, A. S. Irani, J. Gu, D. S. Spencer, N. A. Peppas, Characterization of protein interactions with molecularly imprinted hydrogels that possess engineered affinity for high isoelectric point biomarkers. *J. Biomed. Mater. Res. A* **105**, 1565–1574 (2017).
40. V. P. Pattani, J. W. Tunnell, Nanoparticle-mediated photothermal therapy: A comparative study of heating for different particle types. *Lasers Surg. Med.* **44**, 675–684 (2012).
41. T. Cantu, K. Walsh, V. P. Pattani, A. J. Moy, J. W. Tunnell, J. A. Irvin, T. Betancourt, Conductive polymer-based nanoparticles for laser-mediated photothermal ablation of cancer: Synthesis, characterization, and in vitro evaluation. *Int. J. Nanomedicine* **12**, 615–632 (2017).

Acknowledgments: We gratefully acknowledge H. Culver and D. Spencer for the helpful feedback during this project. We also acknowledge H. Ngyugen and J. Tunnell (UT Austin) for assistance with the photothermal therapy studies. **Funding:** The authors gratefully recognize financial support from the UT-Portugal Collaborative Research Program (CoLAB), the Cockrell Family Chair Foundation, and the NIH (EB022025 to N.A.P.). J.R.C. is supported by an NSF Graduate Research Fellowship (DGE-1610403). A.S.I., E.W.A., A.K.V., and J.X.Z. were supported by undergraduate research fellowships by the UT Austin Office of Undergraduate Research. **Author contributions:** J.R.C. and N.A.P. conceived of the project and wrote the manuscript. J.R.C., A.S.I., E.W.A., C.M.L., and J.X.Z. designed the experiments. J.R.C., A.S.I., E.W.A., C.M.L., J.X.Z., and A.K.V. performed the experiments and analyzed the data. J.R.C. conducted the statistical analyses. **Competing interests:** The authors declare that they have no competing interests. **Data and materials availability:** Additional data validating material compositions, as well as representative images from high-throughput cell experiments, are given in the Supplementary Materials. Additional data from this manuscript can be requested from the corresponding author.

Submitted 30 April 2019
Accepted 26 August 2019
Published 27 September 2019
10.1126/sciadv.aax7946

Citation: J. R. Clegg, A. S. Irani, E. W. Ander, C. M. Ludolph, A. K. Venkataraman, J. X. Zhong, N. A. Peppas, Synthetic networks with tunable responsiveness, biodegradation, and molecular recognition for precision medicine applications. *Sci. Adv.* **5**, eaax7946 (2019).